

Hydrogen Electron Capture in Accreting Neutron Stars and the Resulting g-Mode Oscillation Spectrum

Lars Bildsten and Andrew Cumming
 Department of Physics and Department of Astronomy
 University of California, Berkeley, CA 94720
 bildsten@fire.berkeley.edu, cumming@fire.berkeley.edu

ABSTRACT

We investigate hydrogen electron capture in the ocean of neutron stars accreting at rates $10^{-10} \lesssim \dot{M} \lesssim 10^{-8} M_{\odot} \text{ yr}^{-1}$. These stars burn the accreted hydrogen and helium unstably in the upper atmosphere ($\rho \lesssim 10^6 \text{ g cm}^{-3}$) and accumulate material which usually contains some small amounts of hydrogen (mass fractions are typically $X_r \approx 0.1 - 0.2$) mixed in with the heavier iron group ashes. The subsequent evolution of this matter is determined by compression towards higher densities until electron capture on the hydrogen occurs. We construct steady-state models of the electron captures and the subsequent neutron recombinations onto the heavy nuclei. The density discontinuity from these captures gives rise to a new g-mode (much like a surface wave), which has a lowest order ($l = 1$) frequency of $\approx 35 \text{ Hz} (X_r/0.1)^{1/2}$ on a slowly rotating ($f_s \ll 30 \text{ Hz}$) star. We also discuss, for the first time, a new set of non-radial g-modes unique to these high accretion rate neutron stars. These modes are “trapped” in the finite thickness layer where the electron captures are occurring. The lowest order mode frequencies are in the 1 – 10 Hz range for a few radial nodes on a slowly rotating star. Though the majority of the mode energy resides in the electron capture transition layer, the eigenmode propagates to higher altitudes above the layer and can thus be potentially observable and excited by the nuclear burning or other mechanisms. We also show that the density jump splits the ocean’s thermal modes into two distinct sets, which have most of their energy either above or below the discontinuity. We conclude by discussing how the dispersion relations for these modes are modified for a rapidly rotating ($f_s \gg 30 \text{ Hz}$) neutron star. Whether any of these modes are observable depends on the damping mechanism and the ability to excite them, issues we will address in a future paper.

Subject headings: accretion – nuclear reactions – stars: neutron – stars: oscillations – stars: rotation – X-rays:stars

To appear in *The Astrophysical Journal*, October 20, 1998, Vol. 506

1. Introduction

The liquid core, solid crust and overlying ocean and atmosphere give a neutron star (NS) a very rich spectrum of non-radial oscillations, with acoustic p-modes in the 10 kHz range and a variety of lower frequency g-modes from the toroidal and spheroidal displacements of the crust and surface layers (see McDermott, Van Horn & Hansen 1988 for an overview). Non-radial g-mode oscillations have been studied extensively for isolated and slowly rotating radio pulsars, where the atmosphere and ocean are quiescent. These studies can be separated by the sources of buoyancy that were considered: (1) entropy gradients (McDermott, Van Horn & Scholl 1983; McDermott et al. 1988), (2) density discontinuities (Finn 1987; McDermott 1990; Strohmayer 1993) and (3) mean molecular weight gradients due to β -equilibrium in the core (Reisenegger & Goldreich 1992). Unfortunately, none of these modes have been securely identified with any particular radio pulsar phenomenon.

There are also many accreting neutron stars in binary systems that emit much of their accretion luminosity in X-rays (Lewin, van Paradijs & van den Heuvel 1995). The thermal and compositional structure of these accreting NSs is quite different from that of the isolated radio pulsars, and is far from equilibrium. There have been previous studies of non-radial oscillations in these objects (McDermott & Taam 1987; Bildsten & Cutler 1995 (hereafter BC95); Bildsten, Ushomirsky & Cutler 1996 (hereafter BUC96); Strohmayer & Lee 1996 (hereafter (SL96)). In this paper, we calculate the g-mode spectrum of the ocean of an accreting NS, focusing on the critical effects of hydrogen electron capture.

1.1. Observational Motivation

Much of this work is motivated by the rich spectrum of quasi-periodic oscillations (QPOs) seen in the luminosity of the brightest accreting neutron stars. Utilizing *EXOSAT* data, Hasinger & van der Klis (1989) found that the highest accretion rate objects ($\dot{M} > 10^{-10} M_{\odot} \text{ yr}^{-1}$) fall into two separate classes. Six objects trace out all or part of a “Z” in an X-ray color-color diagram and exhibit time-dependent behavior that correlates with the position along the Z. These “Z sources” have QPO’s in the 15–50 Hz and 5–7 Hz range with up to 10% modulation of the X-ray flux. The other objects fall into separated regions of the color-color diagram and do not show this distinctive QPO phenomenology. These “Atoll sources” accrete at lower rates than the Z sources and exhibit Type I X-ray bursts resulting from the unstable ignition of the accumulated hydrogen and helium (see Bildsten 1998a for a recent review).

The *Rossi X-Ray Timing Explorer (RXTE)* has recently added to this list of QPO phenomenology. Two drifting kHz QPOs are seen in the persistent emission from both Atoll and Z sources, and coherent oscillations have been observed during Type I X-ray bursts from several Atoll sources (see Strohmayer et al. 1996 for an example). In these objects, the kHz QPOs are separated by a frequency identical to that seen in the burst, leading naturally to a beat frequency model in which the difference frequency is the NS spin frequency (Strohmayer et al. 1996). The physical origin of the upper frequency differs in the models (see van der Klis 1998 for a summary), and usually involves the Kepler frequency at some special place in the accretion disk (Kaaret, Ford & Chen 1997; Zhang, Strohmayer & Swank 1997; Miller, Lamb & Psaltis 1998). The inferred spin frequencies are in a remarkably narrow range, 250–500 Hz (White & Zhang 1997; van der Klis 1998; Bildsten 1998b). There are also many QPOs with frequencies less than 100 Hz seen in the Atoll sources. Stella & Vietri (1998) proposed that these might be due to Lense-Thirring precession of the inner accretion disk.

It may be that all of the < 100 Hz and kHz QPOs can be accommodated within the existing models

(see van der Klis 1995, 1998) that use the accretion disk and/or spherical flow to generate the periodic phenomena. However, it is important to pursue non-radial oscillations of the surface layers of the NS as a possible source of some of these periodicities. The predicted frequencies are well-constrained, depend on the underlying NS structure and have well-understood dispersion relations, even when the NS is rapidly rotating (BUC96). This means that the successful identification of a non-radial pulsation with an observed frequency would tell us much about the thermal and compositional makeup of the NS and measure or constrain the rotation rate and magnetic field.

1.2. Accreting Neutron Star Structure and Non-Radial Oscillations

In most cases where stellar pulsations are studied, the underlying stellar model is reasonably well understood and constrained via other observations. Initial theoretical work then consists of finding the adiabatic mode structure and exploring possible excitation mechanisms, usually focusing on the κ -mechanism which relies on opacity changes during the pulsations (see Cox 1980 for an excellent overview). The situation is quite different in an accreting NS. The conditions in the outer layers can change on short timescales, the deep internal structure depends on the accretion history and there is a broader range of excitation possibilities. We now briefly outline the underlying NS structure and the resulting g-mode spectrum.

Figure 1 is a schematic of the NS atmosphere and ocean. For accretion rates $\dot{M} < 10^{-8} M_{\odot} \text{ yr}^{-1}$, the accreted hydrogen (H) and helium (He) rich material burns unstably at a density of $\rho \lesssim 10^6 \text{ g cm}^{-3}$ and within a few hours to days upon arrival on the star. The very high temperatures reached ($T > 10^9 \text{ K}$) during the thermal instability produce elements at and beyond the iron group. The isotopic mixture from this burning is not well known, though it seems to always be the case that a substantial amount of H (the residual mass fraction is typically $X_r \sim 0.1$) remains unburned. The ashes from the burning accumulate on the NS, undergo further compression and form a relativistically degenerate ocean. The hydrogen is eventually depleted by electron captures at $\rho \approx 2 \times 10^7 \text{ g cm}^{-3}$, leading to an abrupt rise in density at that location. At still higher densities, $\rho \sim 10^9\text{--}10^{10} \text{ g cm}^{-3}$, the material crystallizes and forms the crust. The thickness of the ocean is $\approx 10^4 \text{ cm} \ll R$. There is no overt evidence for magnetic fields on these NSs (i.e. none of them are persistent X-ray pulsars) and most arguments about the nature of Type I X-ray bursts limit $B < 10^9 \text{ G}$ (Bildsten 1998a), weak enough not to affect the ocean g-modes (BC95).

There has been prior work on g-modes in the upper atmosphere of the NS, above and around the H/He burning region. McDermott & Taam (1987) calculated g-modes of a bursting atmosphere. SL96 calculated the non-adiabatic mode structure for atmospheres accreting and burning in steady-state and found that g-modes may be excited by the ϵ -mechanism (i.e. by the nuclear burning) when $\dot{M} < 10^{-10} M_{\odot} \text{ yr}^{-1}$. However, steady-state burning does not occur at these low \dot{M} 's, and realistic calculations for the time dependent NS atmosphere have yet to be carried out.

Our focus in this paper is on the adiabatic mode structure in the deep ocean underneath the H/He burning where the thermal time (hours to days) is much longer than the mode period. The g-modes reside in the ocean as they are effectively excluded from the crust by the restoring force from the finite shear modulus there (McDermott et al. 1988; BC95). If the NS is slowly rotating, the dispersion relation for these modes is that for shallow water waves, $\omega^2 \propto k^2$, where $k = (l(l+1))^{1/2}/R$ is the transverse wavenumber and l is the angular eigenvalue. The transverse wavenumber changes if the star is rapidly rotating, but this is easily calculable (BUC96) and it is straightforward to find the g-mode spectrum from the non-rotating calculations.

The different sources of buoyancy yield a rich spectrum of g-modes. The abrupt rise in density associated

with the hydrogen electron capture boundary layer supports a density discontinuity mode of frequency $f_d \approx 35 \text{ Hz}(X_r/0.1)^{1/2}$ for $l = 1$ and $R = 10 \text{ km}$ (equation [31]). The internal buoyancy due to the composition gradient within the electron capture boundary layer creates a new spectrum of modes which are “trapped”. Much of the mode energy is confined to the boundary layer and our WKB estimate of the mode frequency gives $f_{tr} \approx 8.5 \text{ Hz}/n_{tr}(X_r/0.1)^{1/2}$ for $l = 1$ and $R = 10 \text{ km}$ (equation [42]). where n_{tr} is the number of nodes in the boundary layer. There is also a set of thermal g-modes (BC95) in the same frequency range as the trapped modes, which are separated by the density discontinuity into two distinct sets (see §4.3).

1.3. Outline of This Paper

We begin in §2 by explaining the physics of the deep ocean, the electron captures that occur there and the subsequent neutron captures by the heavy nuclei. We introduce a convenient fitting formula for the electron capture rate and use it to generate a series of stellar models for the subsequent seismic investigation. Section 3 summarizes the equations for non-radial oscillations, discusses the various sources of buoyancy in the deep ocean and our method for solving the eigenvalue problem. We present the full spectrum of g-modes for isothermal oceans in §4. There, we show both the modes due to the electron capture discontinuity and the “trapped” modes, and find that the thermal modes are split into two distinct sets by the density discontinuity. We use the WKB approximation to obtain reliable frequency estimates for these modes. We construct a few realistic non-isothermal ocean models in §5 and show their g-mode spectra. We summarize our results in §6 and discuss the effects of rapid rotation and the important issues of mode excitation, damping and transmittal of the signal to the observer.

2. Electron Capture on Hydrogen in Accreting Neutron Stars

Rosenbluth et al. (1973) first noted that accreted matter would undergo electron capture on hydrogen ($e^- + p \rightarrow n + \nu_e$) once high enough densities were reached ($\rho > 10^7 \text{ g cm}^{-3}$) for the electron Fermi energy to exceed the 1293 keV threshold. Hydrogen electron captures have since been studied in two very different contexts in accreting neutron stars. The first is at very low accretion rates, where the thermonuclear consumption of hydrogen (say via the CNO or pp cycle) is so slow that the matter reaches the capture density prior to having burned any hydrogen. In this hydrogen-rich environment, the neutrons created by this process are immediately captured by protons ($p + n \rightarrow D + \gamma$). Further reactions burn this matter to at least helium, releasing 7 MeV per accreted proton. Van Horn & Hansen (1974) modeled transient X-ray sources as the result of electron capture triggered thermonuclear flashes on low mass ($M < 0.15M_\odot$) neutron stars. A variant of this model was later invoked as a possible source of local gamma-ray bursts by Hameury et al. (1982), who found that the accretion rates where the electron capture ignites a thermonuclear instability is comparable to that expected from a lone neutron star steadily accreting from the interstellar medium.

The second context is at the high accretion rates typical for the brightest X-ray sources. In these stars, the matter undergoes unstable H/He burning within a few hours to days of arrival on the NS, long before reaching densities high enough for electron capture. Provided $\dot{M} > \dot{M}_{c2} \approx 10^{-10} M_\odot \text{ yr}^{-1} (Z_{\text{CNO}}/0.01)^{1/2}$ (Bildsten 1998a), the H burning (via the β -limited hot CNO cycle) is thermally stable while the H accumu-

lates. For accretion rates in excess of

$$\dot{M}_{c1} \approx 7 \times 10^{-10} M_{\odot} \text{yr}^{-1} \left(\frac{1.4 M_{\odot}}{M} \right)^{2/9} \left(\frac{R}{10 \text{ km}} \right)^{22/9} \left(\frac{Z_{\text{CNO}}}{0.01} \right)^{13/18}, \quad (1)$$

(Bildsten 1998a) the CNO cycle cannot consume all of the H before the He unstably ignites (Lamb & Lamb 1978; Taam & Picklum 1979; Fujimoto, Hanawa & Miyaji 1981) in a local thermonuclear flash. For $\dot{M}_{c2} < \dot{M} < \dot{M}_{c1}$, the H is completely burned in a stable manner and the accumulated pile of pure He unstably ignites. There are many neutron stars accreting at rates comparable to \dot{M}_{c1} . However, the strong dependence of \dot{M}_{c1} on Z_{CNO} and R makes it difficult to know in which regime a particular star is burning, especially if a large amount of spallation occurs when the infalling matter decelerates at the surface (Bildsten, Salpeter & Wasserman 1992).¹ The ashes from these two types of unstable burning are quite different. In the pure He case, the ashes are mostly ^{56}Ni (Joss 1978; Ayasli & Joss 1982) and there is little to no hydrogen left at densities in excess of 10^6 g cm^{-3} . Things are different when the He ignites and burns in a hydrogen-rich environment ($\dot{M} > \dot{M}_{c1}$), as we now discuss.

During the thermonuclear flash in the mixed H/He regime, hydrogen burning is accelerated by freshly minted seed nuclei produced by He burning, enhancing the local energy release and substantially complicating the nuclear reaction chains. The very high temperatures reached ($T \gtrsim 10^9 \text{ K}$) during the thermal instability produce elements beyond the iron group (Hanawa, Sugimoto & Hashimoto 1983; Wallace & Woosley 1984; Schatz et al. 1997). The isotopic mixture from this burning is still not well known, though everyone agrees that a substantial amount of hydrogen (the residual mass fraction is typically $X_r \sim 0.1\text{--}0.2$) remains unburned (Ayasli & Joss 1982; Woosley & Weaver 1984; Taam et al. 1993; Schatz et al. 1997). As the mix of H and extremely heavy elements accumulates beneath the H/He burning layers, at temperatures in the range $T \approx (2\text{--}5) \times 10^8 \text{ K}$, some proton captures by the heavy nuclei occur (Schatz 1997, private communication). However, the main proton consumption occurs when the matter has been compressed by accretion to densities high enough for hydrogen electron capture (Woosley & Weaver 1984; Fushiki et al. 1992; Taam et al. 1996). Electron capture onto the nuclei themselves occurs at much greater densities and has been discussed previously by Sato (1979), Haensel & Zdunik (1990a, 1990b) and Blaes et al. (1990).

In this section, we discuss the nuclear physics of the electron capture transition layer in the ocean underneath the H/He burning layer for those objects with $\dot{M} > \dot{M}_{c1}$. We find that the neutrons produced by the electron captures recombine with the heavy nuclei, substantially changing the mix of heavy elements in the layer and below. Our present motivation is to calculate the internal buoyancy associated with the composition gradient in the layer where electron captures are occurring, and the resulting spectrum of g-modes. We find trapped g-modes and a density discontinuity g-mode that directly depend on the internal buoyancy of the electron capture transition layer, and thus only arise when hydrogen is present at these large depths. The presence of such g-modes would identify the star as being in the $\dot{M} > \dot{M}_{c1}$ regime.

¹Many of the recent interpretations of the kHz QPO's from these same objects imply that the NS radius is inside the last stable orbit (Kaaret et al. 1997; Zhang et al. 1997), resurrecting some of the original suggestions of Kluzniak & Wagoner (1985) and Kluzniak, Michelson & Wagoner (1990). If true, then spallation might reach the levels found by Bildsten et al. (1992), as the flow can have a large radial component when it finally reaches the surface.

2.1. The Electron Capture Rate for Hydrogen

The electron capture rate for hydrogen (i.e. $e^- + p \rightarrow n + \nu_e$) residing in an electron gas at temperature T with Fermi energy E_F (including electron rest mass) is

$$R_{ec}(E_F, T) = \left(\frac{\ln 2}{ft} \right) I(E_F, T), \quad (2)$$

(Lang 1980) where $ft = 1065$ s as inferred from the measured neutron half-life (Barnett et al. 1996) and the known f value. The function I is a dimensionless phase space integral over the electron energy E ,

$$I(E_F, T) = \frac{1}{(m_e c^2)^5} \int_Q^\infty \frac{E(E^2 - m_e^2 c^4)^{1/2} (E - Q)^2 dE}{1 + \exp[(E - E_F)/k_B T]}, \quad (3)$$

where $Q = (m_n - m_p)c^2 = 1293.318$ keV is the energy threshold for the reaction. We have evaluated the integral in equation (3) and agree with the tabulated rates of Oda et al. (1994) to within 2%. For the purposes of both analytical insight and numerical speed, we now discuss a few limiting forms for the capture rate and present a convenient fitting formula.

Much insight is gained if we assume relativistic electrons and neglect the $m_e^2 c^4$ term in the integral I . There are then two limits to discuss. For $T = 0$, captures only occur once the threshold is exceeded. For values of the Fermi energy slightly above threshold ($E_F - Q \ll Q$), the integral becomes

$$I(E_F, T) \rightarrow \frac{1}{3} \left(\frac{Q}{m_e c^2} \right)^5 \left(\frac{E_F - Q}{Q} \right)^3, \quad \text{for } T = 0 \text{ near threshold.} \quad (4)$$

When $E_F \lesssim Q$, captures only occur if the electrons have a finite temperature. The integral can be approximately found when $Q - E_F \gg k_B T$, giving

$$I(E_F, T) \rightarrow \frac{2Q^2 (k_B T)^3}{(m_e c^2)^5} \exp\left(\frac{E_F - Q}{k_B T} \right), \quad \text{for } Q - E_F \gg k_B T, \quad (5)$$

so that most captured electrons are far out on the thermal tail of the distribution.

These limiting forms motivate a fitting formulae for the rates that we now introduce. Since this might prove a convenient form for others to use, we motivate our choice and discuss how to use it. It represents a modified (and smooth) combination of equations (4) and (5). The electron capture rate is temperature sensitive even above threshold when $E_F - Q \sim k_B T$. We thus add a term $\propto k_B T$ to E_F in equation (4) which provides some thermal “fuzziness” to the Fermi energy. The proportionality constant and Fermi energy to connect the modified equation (4) with the unmodified equation (5) are found by demanding that the rate and its first derivative with respect to E_F (at constant T) are continuous there. This results in the form

$$I \approx \frac{Q^2}{(m_e c^2)^5} \times \begin{cases} 2(k_B T)^3 \exp[(E_F - Q)/k_B T] & E_F < Q + k_B T \ln(9/2) \\ (1/3)(E_F + (3 - \ln 9/2)k_B T - Q)^3 & E_F > Q + k_B T \ln(9/2), \end{cases} \quad (6)$$

which reproduces the electron capture rate within a factor of two over a large range of temperatures and densities. Figure 2 shows the ratio of the true integral (eqn. [3]) to that given by equation (6) for a range of E_F and temperatures of $T_8 = 1, 2, 5, 8$ and 10. Clearly the fit does rather well at representing a function that is changing by orders of magnitude in this range. The growing deviation at $E_F \gg Q$ arises from our neglect of the next order term in equation (4), which is $\propto (E_F - Q)^4$.

We implement this fit by first tabulating (as a function of E_F and T) the ratio of the real answer to the fit. Then, for any E_F and T , we use equation (6) to evaluate I and then find the correction via interpolation

within this pre-made table. This proves to be quite accurate with a relatively small table, as the fitting formula takes care of most of the strong variations in I .

We describe the structure of the hydrogen electron capture transition layer in §2.3, but we can obtain a rough picture of where the electron captures occur by noting that in steady state, the hydrogen depletes when the lifetime to electron capture, $t_{ec} \equiv 1/R_{ec}$, becomes comparable to the time to reach that depth, $t_{accr} \equiv y/\dot{m}$, where \dot{m} is the local accretion rate (mass accreted per unit time per unit area) and $y = p/g$ is the column depth. The local Eddington accretion rate is

$$\dot{m}_{Edd} = \frac{\mu_e m_p c}{\sigma_T R} = 7.5 \times 10^4 \mu_e \left(\frac{R}{10 \text{ km}} \right) \text{ g cm}^{-2} \text{ s}^{-1}, \quad (7)$$

where σ_T is the Thomson cross-section and μ_e is the mean molecular weight per electron. For simplicity, we take \dot{m}_{Edd} to be the value for $\mu_e = 1$ and $R = 10$ km. Figure 3 shows t_{ec} as a function of E_F for many different temperatures. From top to bottom, the solid lines are for $T_8 = 2, 3, 4, 5, 6, 7, 8,$ and 9 . The vertical dashed line displays $E_F = Q$. The lower (upper) dotted line shows t_{accr} for $\dot{m} = \dot{m}_{Edd}$ ($\dot{m} = 0.1\dot{m}_{Edd}$), where, for simplicity, we have assumed the degenerate electrons provide all the pressure. It is clear that for $T_8 \gtrsim 6$ at $\dot{m} = \dot{m}_{Edd}$ and $T_8 \gtrsim 3$ at $\dot{m} = 0.1\dot{m}_{Edd}$, substantial pre-threshold capture occurs, i.e. many protons are consumed while $E_F < Q$. We discuss this further in §2.3.

2.2. The Fate of the Free Neutrons

In the hydrogen-rich environment, the neutrons produced by the electron captures rapidly thermalize via elastic scattering with protons and undergo a radiative capture (free decay is irrelevant for these high densities, as the radiative capture times are $\ll 10^{-10}$ seconds). Woosley & Weaver (1984) and Taam et al. (1996) assumed that the neutrons would capture onto protons, starting a chain of rapid nuclear reactions up to the Fe group. We find that this is not the case. The reaction rate for capture onto protons ($n + p \rightarrow D + \gamma$) is $\langle \sigma v \rangle = 7.3 \times 10^{-20} \text{ cm}^3 \text{ s}^{-1}$ (Caughlan & Fowler 1988), whereas typical rates for neutron captures onto heavy nuclei are 10^{-17} – $10^{-19} \text{ cm}^3 \text{ s}^{-1}$, nearly two orders of magnitude larger. We thus find that, for the hydrogen mass fractions we consider, most neutrons capture onto the heavy nuclei, releasing the typical 7–8 MeV binding energy of a nucleon in a heavy nucleus. For example, from Cowan, Thielemann & Truran (1991), the neutron capture rate for ^{56}Fe is $5.8 \times 10^{-18} \text{ cm}^3 \text{ s}^{-1}$ (at 30 keV), so that neutrons will capture preferentially onto iron rather than protons when their ratio by number is $\lesssim 80$, requiring $X \lesssim 0.58$. Similar conclusions apply to most nuclei we could consider.

The neutron captures substantially modify the isotopic mix of heavy elements. At a particular depth in the transition layer, those elements with larger neutron capture cross sections grow more and more neutron rich until they become β -unstable on a timescale comparable to the flow time across the region (i.e. days, see Figure 3). Since the composition of the ashes from the H/He burning is still unknown, we adopt a simple model in which we assume that prior to electron capture the gas consists of protons, electrons and a *single* species of nucleus of mass Am_p and charge Ze . The mass fraction of protons X is given by $\rho_p = X\rho$, so that the density of nuclei is $\rho_N = (1-X)\rho$ and the local number ratio of protons to nuclei is $n_p/n_N = XA/(1-X)$. The mean molecular weight per electron for this mixture is

$$\frac{n_e m_p}{\rho} \equiv \frac{1}{\mu_e} = X + \frac{Z}{A} (1 - X), \quad (8)$$

where n_e is the electron number density. We assume that only one nuclear species is present at a particular depth. Given the starting values X_r and A_i , the value of X at a particular depth fixes the mass of the

nucleus A due to baryon conservation, $A/(1 - X) = \text{const} = A_i/(1 - X_r)$. Thus A , in some sense, represents the average weight of the nuclei present, and is a continuous variable. The models we discuss throughout this paper are for the “neutron-rich” case in which we neglect β decays and keep Z fixed and let A grow without bound. We have also constructed models in which the nuclei follow the valley of stability, i.e. at a particular depth we choose the most stable Z corresponding to the local value of A . Clearly, the real composition of the layer lies somewhere between these two cases. However, we find that (except for the density discontinuity mode, see §4.1) the adiabatic seismology depends very weakly on the exact nuclear physics in the layer, and so we adopt the “neutron rich” models for simplicity. We have yet to fully explore the rich nuclear physics of this transition layer.

2.3. The Structure of the Hydrogen Electron Capture Boundary Layer

At the accretion rates of interest for the bright X-ray sources, the downward diffusive drift speed of a nucleus in the hydrogen-rich region is much less than the downward flow speed from accretion, $\vec{v} = -v\hat{z} = -\dot{m}\hat{z}/\rho$. The nuclei thus do not have time to settle out (gravitationally separate) from the hydrogen before the electron captures occur. For example (using equation 4.3 from Bildsten, Salpeter & Wasserman 1993), for temperatures in excess of 5×10^8 K, there is no relative diffusion of protons and heavy ions provided $\dot{M} > 10^{-10} M_\odot \text{yr}^{-1}$. Thus there are no relative separations in the continuity equations (Brown & Bildsten 1998), and we construct models of the hydrogen electron capture boundary layer by integrating the continuity equation for protons,

$$\frac{\partial n_p}{\partial t} + \vec{\nabla} \cdot (n_p \vec{v}) = -n_p R_{ec}. \quad (9)$$

We rewrite this equation in terms of the column density, $y = \int \rho(z) dz = p/g$, and the hydrogen mass fraction X , giving

$$\frac{\partial X}{\partial t} + \dot{m} \frac{\partial X}{\partial y} = -X R_{ec}, \quad (10)$$

where we have used the mass continuity equation. In a steady-state, the electron captures are balanced by the accretion flow, so that

$$\dot{m} \frac{dX}{dy} = -X R_{ec}. \quad (11)$$

Since the temperature gradient across the transition layer is small (see §5.1), we first presume the layer is isothermal in our calculations. In this case, equation (11) gives a complete description of the transition layer. We use these isothermal models in §4 to illustrate the spectrum of ocean g-modes. We discuss realistic non-isothermal models of the whole ocean in §5, in which the heat equation must also be integrated. A discussion of the equation of state and the microphysics of the ocean can be found in BC95. The temperature of the ocean is $T_8 \equiv (T/10^8 \text{ K}) \approx 5-7$.

We now make a simple model of the hydrogen electron capture layer at zero temperature. In this case no electron capture occurs until $E_F > Q$. We neglect the electron rest mass, assume the boundary layer is thin, write the pressure as $p = gy = n_e E_F/4$, and use the capture rate of equation (4). We then integrate equation (11) analytically, obtaining $X(E_F) = X(Q) \exp(-B)$, where

$$B \equiv \int_Q^{E_F} \frac{R_{ec}}{\dot{m}} dy \approx \frac{2\pi}{9(hc)^3} \frac{1}{\dot{m}g} \frac{\ln 2}{ft} \left(\frac{Q}{m_e c^2} \right)^5 (E_F - Q)^4. \quad (12)$$

If we measure the characteristic “thickness”, $\Delta E_F = E_F - Q$, of the electron capture layer by the depth at which the hydrogen is 90% depleted, we find

$$\Delta E_F = 172 \text{ keV} \left(\frac{\dot{m}}{\dot{m}_{Edd}} \right)^{1/4} \left(\frac{g}{2 \times 10^{14} \text{ cm s}^{-2}} \right)^{1/4} \left(\frac{Q}{1293 \text{ keV}} \right)^{-5/4} \left(\frac{ft}{1065 \text{ s}} \right)^{1/4}. \quad (13)$$

Integrating the equation of hydrostatic equilibrium, $dz = -dy/\rho$ gives the corresponding physical thickness of the layer,

$$\Delta z = \frac{826 \text{ cm}}{\Sigma} \left(\frac{\dot{m}}{\dot{m}_{Edd}} \right)^{1/4} \left(\frac{g}{2 \times 10^{14} \text{ cm s}^{-2}} \right)^{1/4} \left(\frac{Q}{1293 \text{ keV}} \right)^{-5/4} \left(\frac{ft}{1065 \text{ s}} \right)^{1/4}, \quad (14)$$

where

$$\frac{1}{\Sigma} \approx \frac{Z}{A_i} (1 - X_r) + \frac{(-3/4)!}{5} X_r \approx \left(\frac{1}{\mu_e} \right)_i, \quad (15)$$

and the subscript i denotes initial values, X_r is the initial hydrogen mass fraction, $(-3/4)! = 3.63$, and we have assumed that Z is constant through the layer. We include the scalings with ft and Q in these formulae as they are equally applicable to electron capture layers associated with nuclei at much larger depths. Numerical integrations of equation (11) with the full $T = 0$ equation of state for the electrons and the exact expression for the electron capture rate (equation [3]) find good agreement with both the scalings and prefactors given in equations (13) and (14) ($\lesssim 5\%$ for $\dot{m} \lesssim 10\dot{m}_{Edd}$ after which the term $\propto (E_F - Q)^4$ neglected in equation (4) becomes important).

As shown in Figure 3, at high enough temperatures significant electron capture occurs pre-threshold. For a particular \dot{m} , there is a critical temperature T_c above which this occurs, roughly given by $k_B T_c \sim \Delta E_F$ from equation (13). We accurately estimate T_c by integrating the continuity equation (11) with the *pre-threshold* expression for the electron capture rate (equation [5]). Again neglecting the electron mass, we find that when

$$T_8 > T_c = 7.1 \left(\frac{\dot{m}}{\dot{m}_{Edd}} \right)^{1/4} \left(\frac{g}{2 \times 10^{14} \text{ cm s}^{-2}} \right)^{1/4} \left(\frac{Q}{1293 \text{ keV}} \right)^{-5/4} \left(\frac{ft}{1065 \text{ s}} \right)^{1/4}, \quad (16)$$

more than 50% of the protons have captured electrons pre-threshold. The prefactor in this expression is taken from numerical integration of equation (11) for an isothermal layer with the full electron capture rate (eq. [3]) and equation of state. Figure 4 shows the critical lines in the \dot{m} - T plane for which 50% and 90% of the protons capture pre-threshold. There is excellent agreement with the analytic estimate.

3. Adiabatic Oscillations in the Ocean

Our present focus is on those g-modes that reside predominantly in the liquid ocean that lies beneath the H/He burning layer. The oscillations are adiabatic there since the local thermal time (hours to days) is much longer than the g-mode period. We first discuss the different sources of buoyancy in the ocean and then describe the adiabatic perturbation equations and our method for solving them.

3.1. Sources of Buoyancy

The g-mode frequencies are set by the local buoyancy force, which results from the density contrast between a displaced fluid element and the background fluid. There are two contributions to this density

contrast. The first is thermal buoyancy, which arises because the change in density of the fluid element as it is adiabatically displaced differs from the change in the background density due to the non-isentropic density gradient. The second contribution is from composition gradients. For example, in the hydrogen electron capture layer the timescale for electron capture is much greater than the mode period, so that the perturbed fluid element’s composition is fixed during the pulsation. Because of the large composition gradient in the layer, the perturbed element is heavier than the surroundings and is forced back.

The local buoyancy is measured by the Brunt-Väisälä frequency N , given by

$$N^2 = -g\mathcal{A} = -g \left(\frac{d \ln \rho}{dz} - \frac{1}{\Gamma_1} \frac{d \ln p}{dz} \right) = -g \left(\frac{d \ln \rho}{dz} + \frac{1}{\Gamma_1 h} \right) \quad (17)$$

where $\Gamma_1 \equiv (\partial \ln p / \partial \ln \rho)_s$ is the adiabatic index and \mathcal{A} is the convective discriminant. For a mixture of electrons and ions, in which the pressure is a function of density ρ , mean molecular weight per electron μ_e and mean molecular weight per ion μ_i , we can rewrite \mathcal{A} as

$$\mathcal{A} = \frac{d \ln p}{dz} \left(\frac{1}{\chi_\rho} - \frac{1}{\Gamma_1} \right) - \frac{\chi_T}{\chi_\rho} \frac{d \ln T}{dz} - \frac{\chi_{\mu_e}}{\chi_\rho} \frac{d \ln \mu_e}{dz} - \frac{\chi_{\mu_i}}{\chi_\rho} \frac{d \ln \mu_i}{dz}, \quad (18)$$

where $\chi_Q = (\partial \ln p / \partial \ln Q)$ with the other independent variables held constant. Using the thermodynamic identities $\Gamma_1 = (\Gamma_3 - 1)\chi_T + \chi_\rho$, and $\nabla_{ad} \equiv (\partial \ln T / \partial \ln p)_s = \Gamma_3 - 1/\Gamma_1$ (Cox & Giuli 1968), we obtain

$$\frac{N^2 h}{g} = \frac{\chi_T}{\chi_\rho} \left[\nabla_{ad} - \left(\frac{d \ln T}{d \ln p} \right)_* \right] - \frac{\chi_{\mu_e}}{\chi_\rho} \left(\frac{d \ln \mu_e}{d \ln p} \right)_* - \frac{\chi_{\mu_i}}{\chi_\rho} \left(\frac{d \ln \mu_i}{d \ln p} \right)_*, \quad (19)$$

where the subscript $*$ refers to the stellar model and $h = p/\rho g$ is the local pressure scale height. The first term in this equation is the thermal buoyancy and the remaining terms are contributions from composition gradients. Figure 5 shows the different contributions to N in isothermal models of the ocean. In the electron capture layer, the buoyancy due to the μ_e gradient dominates the other contributions, elsewhere the thermal buoyancy is most important. The buoyancy due to the μ_i gradient is of order the thermal buoyancy in the layer; despite χ_{μ_i} being small (the pressure is insensitive to μ_i) the change in μ_i is typically large across the layer, $\Delta \mu_i / \mu_i \approx 6$. We use isothermal models here for illustrative purposes. In reality, the ocean has a slight temperature gradient (see §5.1), which changes the thermal buoyancy. However, the electron capture transition layer is typically thin enough so that it can be described by a single temperature.

We now make an analytic estimate of the thermal buoyancy in the isothermal case under some simplifying assumptions. First, we use the relation $\nabla_{ad} = \chi_T p / \rho T c_V \Gamma_1$ to write the thermal buoyancy as

$$N_{th}^2 = \frac{\chi_T^2}{\Gamma_1 \chi_\rho} \frac{g^2}{c_V T}, \quad (20)$$

where c_V is the heat capacity at constant volume. There are two contributions to χ_T . At low temperatures, the electron contribution is small, so that χ_T is dominated by the contribution from the ions, $\chi_T \rightarrow \rho k_B T / \mu_i m_p p$ as $T \rightarrow 0$ (see Hansen & Kawaler 1994 for a useful discussion). The heat capacity is

$$c_V = \frac{k_B}{\mu_i m_p} \left(\frac{3}{2} + \pi^2 \frac{\mu_i}{\mu_e} \frac{k_B T}{E_F} \right), \quad (21)$$

where the first (second) term is the contribution from the ions (electrons). For this estimate, we ignore the electron contribution and treat the ions as an ideal gas, neglecting Coulomb corrections to the equation of

state. Our detailed numerical calculations include all of these effects. Taking $\Gamma_1 \approx \chi_\rho \approx 4/3$ for relativistic electrons, the final result is (compare BC95 equation 3.9)

$$N_{\text{th}}^2 h^2 \mu_i = \frac{3k_B T}{8m_p}. \quad (22)$$

This estimate is shown as the dot-dashed line in Figure 5. It performs well at low temperatures, but underestimates the thermal buoyancy at higher temperatures, where the contribution from the electron entropy becomes non-negligible. The non-ideal gas corrections for the ions (for which we use the parametrization of Farouki & Hamaguchi 1993) have little effect on N .

At zero temperature, the thermal buoyancy vanishes and all buoyancy comes from the μ_e gradient. The pressure is entirely from the degenerate electrons, giving $\Gamma_1 = \chi_\rho = -\chi_{\mu_e}$ and $\chi_{\mu_i} = 0$, so that $N^2 = -g d \ln \mu_e / dz$. This form of buoyancy has been studied before in the core of a neutron star where the density dependent β -equilibrium means that μ_e changes with position. Reisenegger & Goldreich (1992) found a new class of core g-modes in the $\lesssim 100$ Hz range from this effect. These modes do not penetrate far into the crust and so most likely have little impact in the neutron star ocean which we are studying.

3.2. Solving the Adiabatic Mode Equations

The equations describing linear adiabatic perturbations of the thin ($h \ll R$) ocean are

$$\frac{d\xi_z}{dz} = \frac{\delta p}{p} \left(\frac{ghk^2}{\omega^2} - \frac{1}{\Gamma_1} \right) + \frac{\xi_z}{\Gamma_1 h} \quad (23)$$

$$\frac{d}{dz} \frac{\delta p}{p} = \frac{\delta p}{p} \frac{1}{h} \left(1 - \frac{1}{\Gamma_1} \right) + \frac{\xi_z}{h} \left(\frac{\omega^2}{g} - \frac{N^2}{g} \right), \quad (24)$$

where ξ_z is the radial displacement of the perturbed fluid element and δp is the Eulerian pressure perturbation. We follow BC95 and use the notation δ to describe an Eulerian perturbation and Δ to describe a Lagrangian perturbation, $\Delta \equiv \delta + \vec{\xi} \cdot \vec{\nabla}$. We adopt the Cowling approximation, in which we neglect perturbations of the local gravity. We use Newtonian gravity and take $g \equiv GM/R^2$. These equations are in the plane-parallel limit since the depth of the ocean is much less than the stellar radius. The horizontal wavenumber is then $k = \sqrt{l(l+1)}/R$ for a slowly rotating star. Bildsten et al. (1996) showed that rapid rotation simply modifies this angular eigenvalue, allowing our calculations to be easily extended to the case of rapid rotation ($f_s \gg$ mode frequency).

Solving the adiabatic mode equations requires h , Γ_1 and N throughout the ocean. BC95 showed that the shear modulus of the crust effectively excludes g-modes because they have large transverse shearing motions. We thus demand that the radial displacement vanishes, $\xi_z = 0$, at the ocean floor where the ions crystallize. This is defined by $\Gamma = \Gamma_m \approx 173$ (Farouki & Hamaguchi 1993), where

$$\Gamma = \frac{Z^2 e^2}{akT} = 113 \frac{\rho_7^{1/3}}{T_8} \left(\frac{Z}{30} \right)^{5/3} \left(\frac{2Z}{A} \right)^{1/3} \quad (25)$$

measures the importance of Coulomb effects. Here a is the average ion spacing, $4\pi a^3 n_i / 3 = 1$, and we presume for simplicity that only a single ion species is present. Assuming relativistic electrons and using the $T = 0$ Fermi energy (very good approximations at the crystallization depth), we find that the crust starts at a column density

$$y_{cr} \approx 1.85 \times 10^{13} \text{ g cm}^{-2} \left(\frac{T_8}{5} \right)^4 \left(\frac{g}{2 \times 10^{14} \text{ cm s}^{-2}} \right)^{-1} \left(\frac{Z}{30} \right)^{-20/3} \left(\frac{\Gamma_m}{173} \right)^4. \quad (26)$$

The ocean can crystallize before hydrogen electron captures occur only if $T_8 < 1 (Z/30)^{5/3}$, an unlikely circumstance at the accretion rates we are considering.

We adopt a “shooting” method for solving the eigenvalue problem. For a particular trial frequency, we integrate from the surface of the ocean to the top of the crust. The boundary condition at the ocean floor, $\xi_z = 0$, is only satisfied when the trial frequency is an eigenvalue of the equations. We start our integrations at an arbitrary place (column depth $y_t = 10^9 \text{ g cm}^{-2}$) beneath the H/He burning layer. We apply the boundary condition there that the Lagrangian pressure perturbation vanishes ($\Delta p = 0$). Although not strictly correct, this boundary condition is reasonable for the low frequency g-modes we discuss, and we find that the mode frequencies are insensitive to changes in the upper boundary condition or starting point for the integrations.²

4. The Spectrum of Ocean g-Modes

The distinct sources of buoyancy in the region beneath the H/He burning yields an extremely rich spectrum of g-modes. The abrupt rise in density from the hydrogen electron captures supports a single density discontinuity mode, and the internal buoyancy due to the composition gradient creates a new spectrum of modes which are “trapped” in the transition layer. There is also a set of thermal modes, as originally described by BC95, which we now find are separated by the density discontinuity and confined to either the upper or lower parts of the ocean.

We use isothermal models with $A_i = 60$ in this section in order to illustrate and explain the physics of the different types of ocean g-modes. The large amount of overlapping frequencies for these modes means that we must first understand them separately before jumping in to the realistic models that include temperature gradients. Our description of the mode spectrum of non-isothermal models in §5 is then much simpler. These stars also have a surface wave or f-mode and acoustic waves or p-modes. These modes, which have frequencies $\gtrsim 10 \text{ kHz}$, penetrate into the crust because they have little transverse shear and are thus not well represented by our thin ocean models and so we do not discuss them further.

4.1. Discontinuity Modes

As Finn (1987) noted in his original study of discontinuity modes in isolated neutron stars, we gain some intuition by first considering waves at the interface of two *constant density, incompressible* fluids. This case can be solved analytically. Since the discontinuity lies closer to the surface of the ocean than the floor, we take the upper fluid (density ρ_+) to have a finite extent H and the lower fluid (density ρ_-) to extend to infinite depth. In the shallow water wave limit ($kH \ll 1$) the discontinuity mode frequency is then

$$\omega_d^2 = gk^2 H \frac{\rho_- - \rho_+}{\rho_-}. \quad (27)$$

² The g-mode frequencies are insensitive to details of the upper boundary, despite there being some mode amplitude there, because they are mainly determined by buoyancy deeper in the ocean. The exceptions are the upper thermal g-modes, and at high temperatures the trapped modes, whose frequencies depend on the thermal buoyancy above the electron capture layer. For example, changing y_t from 10^9 g cm^{-2} to $5 \times 10^8 \text{ g cm}^{-2}$ changes the discontinuity and lower thermal mode frequencies by 1%, the trapped mode frequencies by up to 10% depending on the temperature, and the upper thermal mode frequencies by 20%. We discuss the effect on the upper thermal modes and trapped modes of extending our calculations into the upper atmosphere in §4.2 and §4.3.

We apply this by ignoring the finite thickness of the hydrogen electron capture layer for now (see §4.1.1 for finite thickness models), and considering a simple model, a $T = 0$ ocean with a discontinuity in ρ and μ_e at the place where $E_F = Q$. The buoyancy then vanishes everywhere, except at the discontinuity. To solve this problem, we modified our shooting scheme and applied the matching conditions $\xi_{z+} = \xi_{z-}$ and $\Delta p_+ = \Delta p_-$ across the discontinuity (Finn 1987; McDermott 1990). In these equations, a + (–) refers to a quantity in the upper (lower) part of the ocean. These conditions are physically motivated; ξ_z must be continuous at the discontinuity because of the continuity equation, while Δp must be continuous to avoid infinite acceleration of a fluid element. There is no restriction on the transverse displacement ξ_\perp , and indeed we find a large jump in ξ_\perp across the discontinuity.

Equation (27) motivates a frequency estimate of the density discontinuity mode associated with the electron capture layer. The length scale governing the behavior of the eigenfunction in the *compressible* case is the pressure scale height just above the discontinuity

$$h_+ = \frac{1560 \text{ cm}}{\mu_{e+}} \left(\frac{E_F}{1293 \text{ keV}} \right) \left(\frac{g}{2 \times 10^{14} \text{ cm s}^{-2}} \right)^{-1}, \quad (28)$$

where we neglected the electron mass and assumed relativistic degeneracy. A natural guess for the discontinuity mode frequency is then

$$\omega_d^2 \approx gk^2 h_+ \frac{\rho_- - \rho_+}{\rho_-}, \quad (29)$$

and at fixed pressure $(\rho/\mu_e)_+ = (\rho/\mu_e)_-$, so that (at $T=0$)

$$f_d = 111 \text{ Hz} \left[\left(\frac{1}{\mu_e} \right)_+ - \left(\frac{1}{\mu_e} \right)_- \right]^{1/2} \left(\frac{10 \text{ km}}{R} \right) \left(\frac{l(l+1)}{2} \right)^{1/2}, \quad (30)$$

or for our case of a single ion species,

$$f_d = 35 \text{ Hz} \left(\frac{X_r}{0.1} \right)^{1/2} \left(1 - \frac{\Delta Z}{\Delta A} \right)^{1/2} \left(\frac{10 \text{ km}}{R} \right) \left(\frac{l(l+1)}{2} \right)^{1/2}, \quad (31)$$

where ΔZ and ΔA are the changes in the charge and mass of the nuclei from one side of the discontinuity to the other. The prefactors in equations (30) and (31) are from our numerical calculations. The scalings found are as predicted by equation (29). The mode frequency is insensitive to the position of the surface or floor of the ocean as long as they lie more than a few scale heights away from the discontinuity. This is as we expect in the spirit of our guess above; it is the shortest length scale near the discontinuity which dominates the mode eigenfunctions and sets the mode frequency in the limit of $kH \ll 1$.

The left panel in Figure 6 displays the eigenfunctions for a $T = 0$ density discontinuity mode with $X_r = 0.1$. The density profile used for this mode is the dotted line in Figure 7. There is a large contrast (and actually a sign change) in the amplitude of the transverse displacement above and below the discontinuity. This means that almost all of the mode energy lies in the upper part of the ocean, above the boundary layer. The radial displacement has maximum amplitude at the discontinuity, and decays towards the ocean surface and floor.

4.1.1. Discontinuity Modes with a Finite-Thickness Transition Layer

We now consider models with a finite thickness hydrogen electron capture layer that are appropriate for the accretion rates we are considering. In these models, the density continuously changes across the layer.

The solid lines in Figure 7 show the density as a function of position for three different accretion rates when $T_8 = 5$ and $X_r = 0.1$. The dashed lines show the changing mass fraction of hydrogen. The dotted line shows the case where all the captures occur at $E_F = Q$ and $T = 0$. Clearly, such a sharp discontinuity is no longer present at these high accretion rates. However, we find that the density discontinuity mode has the same frequency as the discontinuous model as long as the electron captures occur over less than a pressure scale height. The eigenfunction is also qualitatively the same, except that the boundary layer is resolved, for example there is a large transverse shear as ξ_\perp rapidly decreases³, and the radial node which at $T = 0$ lies immediately below the discontinuity is moved deeper in the ocean. The right panel of Figure 6 shows a typical discontinuity mode in an isothermal ocean.

It might come as a surprise that the same discontinuity mode appears in both the simple model and the models with a finite thickness electron capture layer. Indeed, one case involves matching conditions across the discontinuity while the other involves smoothly integrating the adiabatic mode equations through the layer. We now show that, in the limit of a thin layer, the matching conditions can be recovered by integrating the mode equations through the electron capture layer. We use the transverse momentum equation, $ik\delta p = \rho\omega^2\xi_\perp$ to transform the dependent variables in the adiabatic mode equations (23) and (24) from $(\delta p/p, \xi_z)$ to (ξ_\perp, ξ_z) , finding

$$\frac{d\xi_z}{dz} = \frac{\xi_z}{\Gamma_1 h} + ik\xi_\perp \left(\frac{\omega^2}{c_s^2 k^2} - 1 \right) \quad (32)$$

$$\frac{d\xi_\perp}{dz} = \frac{N^2 \xi_\perp}{g} + ik\xi_z \left(1 - \frac{N^2}{\omega^2} \right), \quad (33)$$

where c_s is the adiabatic sound speed, $c_s^2 \equiv \Gamma_1 g h$. The discontinuity mode has $\omega_d^2 \ll N^2$, $\omega_d^2 \ll c_s^2 k^2$ and $\xi_z \lesssim kh\xi_\perp$, allowing equation (32) to be approximated as

$$\frac{d\xi_z}{dz} = \frac{\xi_z}{h} \left[\frac{1}{\Gamma_1} - i(kh) \left(\frac{\xi_\perp}{\xi_z} \right) \right] = \mathcal{O} \left(\frac{\xi_z}{h} \right). \quad (34)$$

Integrating this through the transition layer gives

$$\xi_{z-} = \xi_{z+} \left[1 + \mathcal{O} \left(\frac{\Delta z}{h} \right) \right], \quad (35)$$

where $\Delta z \ll h$ is the thickness of the layer. The pressure is nearly constant within the electron capture layer as ρ and μ_e trade against each other. In other words the density scale height is much less than the pressure scale height, $h(d \ln \rho / dz) \gg 1$, so we simplify

$$N^2 = -g \left(\frac{d \ln \rho}{dz} + \frac{1}{\Gamma_1 h} \right) \approx -g \frac{d \ln \rho}{dz}, \quad (36)$$

and equation (33) becomes

$$\frac{d\xi_\perp}{dz} = -\frac{d \ln \rho}{dz} \left(\xi_\perp - i \frac{kg}{\omega^2} \xi_z \right). \quad (37)$$

³ One might worry that the large transverse shear in the transition layer would be unstable to a Kelvin-Helmholtz type instability. At the accretion rates and X_r 's we consider, however, we find that the shear in the transition layer is stabilized by the buoyancy there. The Richardson number in the layer is always much greater than 1/4 as long as the transverse displacement at the top of the ocean is less than a stellar radius.

Using the fact that ξ_z is nearly constant in the layer, we integrate through the layer using the transverse momentum equation to find

$$\frac{h_+ \Delta p_+}{h_- \Delta p_-} = \frac{\rho_-}{\rho_+}. \quad (38)$$

But since the pressure is constant, so is ρh , giving us

$$\Delta p_- = \Delta p_+ \left[1 + \mathcal{O} \left(\frac{\Delta z}{h} \right) \right]. \quad (39)$$

For a thin boundary layer ($\Delta z \ll h$), equations (35) and (39) are just the matching conditions from our simple model.

4.1.2. Dependence of f_d on Temperature and Accretion Rate

The discontinuity mode frequency differs slightly from the simple estimate above (equation [31]) due to three different effects: (1) pre-threshold electron captures change the position of the layer in the ocean, (2) thermal buoyancy provides some extra restoring force above and below the transition layer, and (3) at high \dot{m} and T the thickness of the layer can exceed the local scale height. However, we found that the dependence on these factors is rather weak and typically is not larger than 20–30% for an order of magnitude change in \dot{m} or T .

Figure 8 shows the effect of \dot{m} and T on f_d for isothermal oceans with $X_r = 0.1$. At low accretion rates ($\dot{m} \lesssim 0.05 \dot{m}_{\text{Edd}}$), increasing T_8 *decreases* f_d because pre-threshold captures move the electron capture layer upwards in the ocean, decreasing the scale height at the transition layer. At higher \dot{m} 's, f_d *increases* with T_8 because of increasing thermal buoyancy and thickness of the transition layer. The effect of thermal buoyancy is shown by the dotted lines, which show f_d for models where the thermal buoyancy is omitted. The effect of increasing layer thickness is shown by the $T = 0$ line, which can be fit by a simple $\dot{m}^{1/4}$ scaling, as suggested by equation (14), for the physical width of the electron capture layer. In the relevant temperature range of $T_8 \approx 5\text{--}7$, we find that the frequency scales roughly as $f_d \propto \dot{m}^{1/36}$.

The models shown in Figure 8 are equilibrium models of the ocean. In reality, the electron capture layer is unlikely to be in complete thermal balance with the current value of the hydrogen mass fraction, as the thermal time there (minutes to hours) is much less than the accretion time (hours to days). The response of the mode frequencies to changes in temperature on a short timescale will be determined by changes in the thermal buoyancy and not in the structure of the layer itself.

4.2. Trapped Modes within the Transition Layer

We have also found a new set of g-modes which reside within the electron capture layer. The restoring force for these modes comes mainly from the buoyancy within the layer due to the composition gradient, and so they exist even when $T = 0$. However, their existence depends on the finite thickness of the electron capture layer, which is a characteristic of the layers in accreting neutron stars. These modes were not found in the density discontinuity mode studies of isolated neutron stars (Finn 1987; McDermott 1990; Strohmayer 1993), as in that environment the electron capture transitions were presumed (most likely safely) to be sharp. Though the modes propagate above and beyond the transition layer, we will refer to them as “trapped” modes, as we can understand their frequencies depending on how many nodes are present in the transition layer.

Figure 9 shows the $n_{tr} = 1$ and $n_{tr} = 2$ trapped modes in a $T = 0$ ocean, where n_{tr} is the number of radial nodes *within the transition layer*. Almost all of the mode energy lies in the transition layer in the unphysical $T = 0$ limit. The transverse displacement is constant in the upper and lower oceans because N vanishes there and the mode is mostly transverse (see eq. [33]). When there are many radial nodes per scale height ($k_z h \gg 1$) we can estimate the mode frequencies in the WKB limit. The coefficients in the adiabatic mode equations (23) and (24) are then constant and are integrated to obtain the dispersion relation for high order g-modes, $k_z^2 = N^2 k^2 / \omega^2$. We require that there be an integer number of wavelengths, $\int k_z dz = n\pi$, giving the frequency of the n 'th mode as

$$f_n \approx \frac{k}{2\pi^2} \frac{1}{n} \int N dz = \frac{k}{2\pi^2} \frac{1}{n} \int N h d \ln y. \quad (40)$$

The trapped mode frequencies are set by the internal buoyancy due to the composition gradient in the transition layer. For nearly all cases we are considering, this dominates the thermal buoyancy within the layer (see Figure 5), so that N in that region is given by

$$N^2 = \frac{g}{h} \frac{d \ln \mu_e}{d \ln y} = -\frac{g}{h} \mu_e X \frac{d \ln X}{d \ln y}, \quad (41)$$

where we have presumed (for simplicity) that the nuclear charge Z is constant so that μ_e is only a function of X . Adopting a relativistic equation of state, we use the solution $X(E_F) = X(Q) \exp(-B)$, with B given by equation (12), to evaluate N . Integrating through the transition layer gives the convenient formula

$$f_{tr} = \frac{8.5 \text{ Hz}}{n_{tr}} \left(\frac{X_r}{0.1} \right)^{1/2} \left(\frac{\dot{m}}{\dot{m}_{\text{Edd}}} \frac{g}{2 \times 10^{14} \text{ cm s}^{-2}} \frac{ft}{1065 \text{ s}} \right)^{1/8} \left(\frac{1293 \text{ keV}}{Q} \right)^{5/8} \times \left(\frac{10 \text{ km}}{R} \right) \left(\frac{l(l+1)}{2} \right)^{1/2}, \quad (42)$$

where we insert the prefactor found numerically. The analytic prefactor is close to that found numerically, and is a function of fundamental constants. We also show the scaling with ft and Q , since this formula is equally applicable to other electron capture boundary layers.

We find excellent agreement between the predicted scalings and our numerical results. Figure 10 compares the analytic and numerical scalings with \dot{m} and X_r for a range of n_{tr} values. The left panel displays the first eight trapped mode frequencies as a function of X_r for a fixed accretion rate ($\dot{m} = \dot{m}_{\text{Edd}}$) and $T = 0$. The filled triangles are our numerical results and the solid lines are from equation (42). The right panel of Figure 10 compares the \dot{m} scaling for $X_r = 0.1$ and $T = 0$. It is clear that the WKB formulation gives an excellent answer at high n_{tr} and is reasonable at low n_{tr} as well. We close by noting that the ratio of the discontinuity mode frequency to a trapped mode frequencies is nearly independent of everything

$$\frac{f_d}{f_{tr}} = 4n_{tr} \left(1 - \frac{\Delta Z}{\Delta A} \right)^{1/2} \left(\frac{\dot{m}}{\dot{m}_{\text{Edd}}} \right)^{-1/8} \left(\frac{g}{2 \times 10^{14} \text{ g cm}^{-2}} \right)^{-1/8}, \quad (43)$$

and thus might be an excellent observational discriminant.

For $T > 0$, the effect of thermal buoyancy is to allow these modes to extend into the upper ocean and atmosphere. Figure 11 shows the $n_{tr} = 1$ and $n_{tr} = 2$ trapped modes in an isothermal ocean with $T_8 = 5$. The frequencies are not much different from their $T = 0$ values. The transverse displacement in the electron capture layer is less than at $T = 0$ because the thermal buoyancy above the layer makes ξ_{\perp} decay with depth. The mode extension into the upper ocean is critical for excitation of the trapped modes, particularly as the

mode then extends into the H/He burning layer. We are currently investigating this possibility, as well as excitation from the electron captures themselves. The thermal buoyancy is also larger at lower pressures and this will increase the mode frequency when the mode amplitude is significant in the upper atmosphere. We now show that at finite temperatures there is the additional complication due to the coincidence that the thermal modes are “mixed” with these trapped modes, at least in frequency space.

4.3. Thermal Modes

The thermal buoyancy throughout the deep ocean of degenerate electrons produces a set of thermal g-modes (BC95). These modes were extensively discussed by BC95, who pointed out the weak frequency dependence on the depth of the ocean, a convenient situation since the depth depends so strongly on uncertain quantities (see eq. [26]). Just for completeness, we estimate the thermal g-mode frequencies in the WKB limit by integrating equation (40). In a region where μ_i is constant and the electrons are very degenerate, equation (22) gives $N^2 h^2 \approx 3k_B T / 8\mu_i m_p = \text{constant}$ and the integration simply gives

$$f_{th} = \frac{4.0 \text{ Hz}}{n} \left(\frac{T_8}{\mu_i} \right)^{1/2} \ln \left(\frac{y_b}{y_t} \right) \left(\frac{10 \text{ km}}{R} \right) \left(\frac{l(l+1)}{2} \right)^{1/2}, \quad (44)$$

where y_t (y_b) is the column depth at the top (bottom) of the ocean. The frequencies depends most strongly on the temperature and ion mean molecular weight and only logarithmically on the physical thickness of the ocean.

We find that the density discontinuity due to the hydrogen electron captures divides the thermal g-modes into two types, which we call the upper and lower thermal modes. Examples are shown in Figure 12 for an isothermal ocean with $T_8 = 5$, $\dot{m} = \dot{m}_{\text{Edd}}$ and $X_r = 0.1$. The upper thermal modes (left panel in Figure 12) have most of their energy *above* the electron capture layer. The layer acts as a floor for these modes and there is a node in the radial displacement there, just as there would be if we demanded our normal bottom boundary condition. This is not by design, but is rather how the modes behave. This motivates us to use our WKB estimate (eq. [44]) and insert typical values for μ_i and column depths in order to estimate these upper thermal mode frequencies

$$f_{\text{th,upper}} = \frac{9.0 \text{ Hz}}{n_{\text{upper}}} \left(\frac{T_8}{5} \frac{9}{\mu_i} \right)^{1/2} \ln \left[\left(\frac{y_b}{2 \times 10^{10} \text{ g cm}^{-2}} \right) \left(\frac{y_t}{10^9 \text{ g cm}^{-2}} \right)^{-1} \right] \times \left(\frac{10 \text{ km}}{R} \right) \left(\frac{l(l+1)}{2} \right)^{1/2}. \quad (45)$$

The lower thermal modes (example in the right panel of Figure 12) have most of their energy *beneath* the electron capture layer. We find that the Lagrangian pressure perturbation has a node at the electron capture layer, just as it would if we put our traditional top boundary condition at that location. In that sense, the layer acts as a surface for these modes. Equation (44) then gives the lower thermal mode frequencies as

$$f_{\text{th,lower}} = \frac{7.2 \text{ Hz}}{n_{\text{lower}}} \left(\frac{T_8}{5} \frac{60}{\mu_i} \right)^{1/2} \ln \left[\left(\frac{y_b}{10^{13} \text{ g cm}^{-2}} \right) \left(\frac{y_t}{2 \times 10^{10} \text{ g cm}^{-2}} \right)^{-1} \right] \times \left(\frac{10 \text{ km}}{R} \right) \left(\frac{l(l+1)}{2} \right)^{1/2}, \quad (46)$$

where we have put in the top column as the electron capture layer and the bottom at the crystallization depth. We also took $\mu_i = 60$, as no hydrogen is present at these depths. The upper and lower thermal mode frequencies are similar because the difference in μ_i above and below the electron capture layer is compensated by the greater depth of the ocean beneath the electron layer than above. Here n_{lower} (n_{upper}) is the number of radial nodes below (above) the electron capture transition layer.

The thermal mode spectrum is split because the jump in density and N^2 across the transition layer creates an impedance mismatch, so that an impinging wave is partially reflected by the transition layer. This phenomenon is seen in so-called “mode trapping” in white dwarfs, in which thermal modes are “trapped” in the thin hydrogen or helium layers at the surface of the star (Winget, Van Horn & Hansen 1981; Brassard et al. 1992). These modes (analogous to our upper thermal modes) are believed to be preferentially excited. It may well be that something similar happens in our case. Just like the trapped modes (§4.2), the upper thermal modes have significant mode energy near the upper boundary, and so it is likely that they will extend upwards into the upper atmosphere. We are currently investigating this as we consider excitation mechanisms. The thermal buoyancy in the upper atmosphere will most likely increase the frequency of the upper thermal modes. For example, Strohmayer & Lee (1996) investigated the seismology of an atmosphere accreting and burning in steady state and found thermal g-modes of frequency approximately 50Hz for comparable accretion rates. The lower thermal modes are more or less confined to the deeper regions of the star. They do propagate upwards, but not enough to have their frequencies modified by any atmospheric physics.

4.4. Avoided Crossings and Mode Identification

To conclude our discussion of isothermal models, we show in Figure 13 the spectrum of $l = 1$ modes in an isothermal ocean with $T_8 = 5$, $\dot{m} = \dot{m}_{Edd}$ and $X_r = 0.1$, our fiducial isothermal model. Each horizontal line shows a mode frequency. The highest frequency mode is the discontinuity mode, lower frequency modes are trapped and thermal modes. The positions of the radial nodes in each mode are shown as circles and triangles. The dashed vertical lines approximately bound the electron capture layer, showing where the thermal and composition gradient contributions to N^2 are equal.

Diagrams like the one in Figure 13 help greatly in mode classification. The type of a given mode can be inferred more or less by where the extra node is placed as one jumps from mode to mode down the diagram. Trapped modes have a new node added within the transition layer and this node remains there as one moves down the diagram. These nodes are marked with circles. A lower (upper) thermal mode has a new node placed at the bottom (top) of the transition layer and this node then moves downwards (upwards) in the ocean as one moves down the diagram. These nodes are marked with downward-pointing (upward-pointing) triangles. Thus in Figure 13, the types of modes from top to bottom are d,u,t,l,u,l,t,l,u,t,l where d is for discontinuity, t is for trapped and u(l) is for an upper (lower) thermal mode. This method of classifying nodes greatly eases the mode identification problem. In particular, it helps to distinguish between trapped and upper thermal modes, whose eigenfunctions may be very similar⁴ (for example, compare Figures 11 and 12). It is not completely reliable however, as it is complicated by the mixing of mode eigenfunctions near avoided crossings, as we now discuss.

⁴This is because the thermal buoyancy above the transition layer begins to play a role in setting the trapped mode frequencies. The trapped and upper thermal modes remain two distinct sets of modes, however. For example, their frequencies depend differently on the position of the upper boundary.

It is by complete coincidence that the upper and lower thermal modes are at a similar frequency to the trapped modes. The frequencies of these modes depend differently on \dot{m} , T_8 , and X_r , leading to “avoided crossings” whenever two mode frequencies try to cross and an accidental degeneracy arises. Avoided crossings were found for non-radial oscillations in massive main sequence stars by Osaki (1975), and in the neutron star context by Carroll et al. (1986), who found avoided crossings between g-modes and p-modes in their investigation of non-radial oscillations in the presence of strong magnetic fields ($B \gtrsim 10^{11}$ G).

Avoided crossings can be seen in Figure 14 which shows the frequencies of the discontinuity mode (upper solid line) and several thermal and trapped modes as a function of X_r for an isothermal ocean with $T_8 = 5$ and $\dot{m} = \dot{m}_{\text{Edd}}$. Each solid line is the frequency of a mode with a fixed number of radial nodes n , and, as expected, the frequency always decreases as n increases. The different dependencies of the mode frequencies on X_r result in a series of avoided crossings. Along a solid line, the number of radial nodes is conserved, but the character of the mode (upper thermal, lower thermal or trapped, denoted by an upward-pointing triangle, downward-pointing triangle or circle) may change. The dot-dashed line shows the $X_r^{1/2}$ scaling expected for the trapped and discontinuity mode frequencies. The thermal mode frequencies scale as $\mu_i^{-1/2}$. For the lower thermal modes (dashed line) this gives a decreasing frequency with X_r because μ_i in the lower ocean increases with X_r . For the upper thermal modes (dotted line) the scaling is $\propto X_r^{1/2}$ at high X_r but levels out at low X_r . On average, the different types of modes follow the predicted scalings by changing n in avoided crossings. Locally, however, the behaviour with X_r may be quite different.

Figure 15 is a similar diagram to Figure 14 in which we show the dependence of the mode frequencies on temperature in an isothermal ocean with $\dot{m} = \dot{m}_{\text{Edd}}$ and $X_r = 0.1$. Again, each solid line is for a mode with a fixed number of radial nodes n , and, as before, the different scalings of the mode frequencies with temperature yield avoided crossings. The dot-dashed line shows the $T^{1/2}$ frequency scaling of the thermal modes. The dashed line shows the frequency of the $n = 1$ trapped mode when thermal buoyancy is not included. It shows how the frequency of the trapped mode changes due to changes in the structure of the boundary layer. Again, on average the modes follow the expected scaling with T , but not necessarily locally.

Avoided crossings have been discussed by Aizenman et al. (1977), Gabriel (1980) and Christensen-Dalsgaard (1981) using an approach analogous to degenerate perturbation theory in quantum mechanics. In this picture the frequency splitting at the point of closest approach during a crossing is proportional to the “overlap” between the eigenfunctions of the two modes (the off-diagonal matrix element in quantum mechanics). This may explain why an avoided crossing between an upper thermal mode and a trapped mode has a larger frequency splitting than an avoided crossing involving a lower thermal mode in Figures 14 and 15. The “overlap” between upper thermal mode and trapped mode eigenfunctions is greater than between an upper thermal or trapped mode and a lower thermal mode.

During an avoided crossing, the mode eigenfunctions are mixed. We show this in Figure 16 in which we take the avoided crossing which is circled in Figure 15, and show the energy density of the two modes before, during and after the avoided crossing. This crossing is between a lower thermal mode and a trapped mode. The $n = 4$ and $n = 5$ mode energy densities are shown as a function of column depth for a range of temperatures from top to bottom. The circles show the position of the radial nodes. At $T_8 = 1.3$, the lower frequency $n = 5$ mode is a lower thermal mode, while the higher frequency $n = 4$ mode is a trapped mode. At the avoided crossing, $T_8 \approx 1.7$, the mode eigenfunctions are qualitatively similar, differing only by a node. At higher temperature, $T_8 = 2.3$, the two modes have exchanged characters. The lower frequency $n = 5$ mode is now a trapped mode while the higher frequency $n = 4$ mode is a lower thermal mode. The mixing of mode eigenfunctions may have implications for mode excitation, allowing exchange of energy between the two modes (for example, see Christensen-Dalsgaard 1981).

5. Non-Isothermal Ocean Models

Up to this point we have presumed that the ocean is isothermal and considered the temperature to be a free parameter. We now construct non-isothermal models of the ocean by integrating the heat equation (see Brown & Bildsten 1998) through the ocean. There are several sources of energy that contribute to the heat flux in the ocean. The first is the energy released when the neutrons from the hydrogen electron captures combine with the heavy nuclei, roughly $E_H \approx 7 \times 10^{18}$ ergs $\text{g}^{-1} \approx 7$ MeV per accreted nucleon. The second is the energy released as matter falls downwards (or what is sometimes called “compressional heating”), $E_{\text{comp}} \sim k_B T / \mu_i m_p$. Finally, there is energy released in the deep crust by nuclear electron captures and pycnonuclear reactions. Most of this energy (about an MeV per accreted nucleon, Haensel & Zdunik, 1990a) goes into the NS core and is lost via neutrinos, about 10% ($E_{cr} \sim 0.1$ MeV per accreted nucleon) flows upwards through the ocean (Brown & Bildsten 1998). The total heat flux above the electron captures (at say $y \approx 10^9$ g cm^{-2}) is

$$F_{\text{deep}} \approx \dot{m}(E_H X_r + E_{\text{comp}} + E_{cr}). \quad (47)$$

The largest uncertainty in F_{deep} is the amount of hydrogen left unburned and advected downward, X_r (Taam et al. 1996; Schatz et al. 1997b). As we show in this section (in agreement with Taam et al. 1996), for typical values of $X_r \sim 0.1$ and high accretion rates the region between the H/He burning layer and the hydrogen electron captures has a substantial temperature gradient. The other contributions to F_{deep} are typically not large enough to require a substantial temperature gradient (BC95) at sub-Eddington accretion rates, especially in the relativistic ocean underneath the hydrogen electron captures.

Even when F_{deep} is known and nuclear reactions beyond electron capture are ignored⁵, there are still additional uncertainties. One is the radiative opacity for this complicated mixture of elements. For pure iron at the depth where the hydrogen electron captures are occurring, the predominant heat transport mechanism would be electron conduction (Gudmundsson, Pethick, & Epstein 1983). Thus for simplicity, we neglect radiative heat transport and assume that all the heat is carried by electron conduction. For the conductive opacities, we use the results of Yakovlev & Urpin (1980) for electron-ion collisions, and the fit of Potekhin et al. (1997) for electron-electron collisions. An additional uncertainty is the choice of temperature at the top of the ocean when the H/He burning is time dependent. This is because the separation between the electron capture region and the burning location is not far enough that a simple radiative-zero like solution applies, at least when $T \gtrsim 5 \times 10^8 \text{K}$ at the electron capture depth.

5.1. A Few Illustrative Models

In order to illustrate the effects of F_{deep} , we show in Figure 17 the temperature, hydrogen mass fraction and density as a function of column depth for models with $\dot{m} = 0.1 \dot{m}_{\text{Edd}}$ and $X_r = 0.2, 0.1$ and 0.05 (from top to bottom in the T and X panels). In the density panel, the curve with the highest density at the largest column depth has $X_r = 0.2$. These models have the outer boundary condition $T = 2 \times 10^8$ K at $y = 10^9$ g cm^{-2} and, for simplicity, we set $E_{\text{comp}} = 0$ and $E_{cr} = 10^{17}$ erg $\text{g}^{-1} \approx 0.1$ MeV per accreted nucleon. The initial nucleus has $A_i = 60, Z_i = 30$ and is allowed to become arbitrarily neutron rich. The

⁵For the purposes of illustration in this section, we persist with our simple model of electron capture followed by neutron capture onto a single type of nucleus. There is no reason to undertake a more complete treatment of the neutron captures/ β -decays and the possibility of direct proton captures onto the nuclei when $T > 10^9$ K until we have better knowledge of the nuclear mix from the H/He burning.

flux at depths far below the electron capture region is $F_{\text{bottom}} = \dot{m}E_{cr} = 7.5 \times 10^{20} \text{ erg s}^{-1} \text{ cm}^{-2}$. It is clear that, for these values of X_r , the ocean is substantially hotter than if there were no hydrogen present. At this accretion rate, the ocean is nearly isothermal below the hydrogen electron captures. Most of the electron captures are post-threshold ($E_F > Q$) and occur 15–30 days after the matter has arrived on the star.

Figure 18 shows models with a higher accretion rate, $\dot{m} = 0.5\dot{m}_{\text{Edd}}$, and an outer boundary condition of $T = 4 \times 10^8 \text{ K}$ at $y = 10^9 \text{ g cm}^{-2}$. The other variables are the same as in the previous example. The enhanced flux due to the higher accretion rate (see eq. [47]) makes these models much hotter than the lower accretion rate ones. We may have slightly overestimated the temperature at these high \dot{m} 's, since for $T \gtrsim 10^9 \text{ K}$, radiation may start to carry a significant fraction of the flux. Many of the electron captures for the $X_r = 0.2$ and $X_r = 0.1$ cases occur pre-threshold ($E_F < Q$). For the $X_r = 0.2$ case, one half of the hydrogen is depleted only 2.5 days after arriving on the NS.

At these high temperatures ($> 10^9 \text{ K}$) it is important to consider neutrino cooling. Using the formulae given by Schinder et al. (1987), we find that, even for the hottest model we consider here ($\dot{m} = 0.5$, $X_r = 0.2$), neutrino cooling is unimportant at the depth of the hydrogen electron captures. It is certainly very important at greater depths however (Brown & Bildsten 1998). Once $y \sim E_{cr}\dot{m}/\epsilon_\nu$, where ϵ_ν is the neutrino cooling rate in $\text{erg g}^{-1} \text{ s}^{-1}$, the temperature gradient changes direction and heat starts to flow into the core, a possibility we neglect for now. For $\dot{m} = 0.5$, this depth is $y \sim 10^{13}\text{--}10^{14} \text{ g cm}^{-2}$, near the bottom of the ocean. At higher \dot{m} 's or X_r 's neutrino cooling will become important at even lower column depths than this, although we stress again that at higher temperatures it becomes important to include the radiative opacity.

How does the hydrogen electron capture transition layer compare to the isothermal cases we calculated previously? Figures 17 and 18 show that the transition layer itself is nearly isothermal. For example, even in the model with $\dot{m} = 0.5$ and $X_r = 0.2$, the temperature changes by a factor of only 10% across the transition layer. We thus characterise the structure of the layer by the temperature at, say, the place where one half of the hydrogen is depleted. For example, the hydrogen mass fraction X in the non-isothermal model with $\dot{m} = 0.5$ and $X_r = 0.1$ agrees to within 10% at each depth with an isothermal model with $T = 10^9 \text{ K}$ and the same \dot{m} and X_r .

These examples are intended to illustrate the large impact of the hydrogen electron captures (Taam et al. 1996) on the deep structure of the neutron star. Much more work is needed on the products of H/He burning before any definitive results can be stated. However, we hope we have strengthened the case of Taam et al. (1996) that even small amounts of residual hydrogen at high \dot{m} 's can play an important role. We now describe the g-mode spectra of these non-isothermal models.

5.2. g-Mode Spectra for Non-Isothermal Models

The g-mode spectra of non-isothermal models of the ocean are easy to understand in the context of our study of isothermal ocean g-modes in §4. The g-mode spectra for the $\dot{m} = 0.1, X_r = 0.05$ and $\dot{m} = 0.1, X_r = 0.1$ models discussed above are shown in Figure 19. The discontinuity mode frequency is insensitive to details of the structure of the transition layer and depends mainly on X_r . It is given accurately by equation (31). The lower thermal mode frequencies are set by the thermal buoyancy in the ocean below the transition layer, which is almost isothermal. The frequencies are almost the same as the lower thermal mode frequencies in an isothermal ocean with a temperature equal to that just below the transition layer. The discontinuity and lower thermal mode frequencies are insensitive to details of the upper boundary and

thermal buoyancy above the transition layer. This is not true of the upper thermal and (to a lesser extent) the trapped modes. Hence we expect that their frequencies will change as we extend our models into the upper atmosphere. Also, we have not included radiative opacity which becomes important near the upper boundary and will reduce the temperature gradient there. In Figure 19 we show the predicted frequency increases due to temperature for the thermal modes ($T^{1/2}$ scaling) and due to X_r for the trapped modes ($X^{1/2}$) by vertical bars. These simple scalings predict the difference in frequencies between the left and right panels of Figure 19 fairly well.

As a further example, we have reconstructed one of the models of Taam et al. (1996). They followed the time dependent evolution of models with accretion rates ranging from 0.1–1 times the Eddington rate. All of these models had substantial residual hydrogen, ranging at the highest \dot{m} 's from $X_r = 0.08$ – 0.21 . Their neutron star had $M = 1.4M_\odot$ and $R = 9.1$ km and the initial heavy nucleus was iron ($A_i = 56, Z_i = 26$). We chose model 8 from their tables 1 & 2 which has $X_r = 0.137$ and $\dot{m} = 0.1\dot{m}_{Edd}$, and varied our outer boundary condition until we matched their stated deep temperature. We then calculated the g-mode spectrum of this model. This is shown in Figure 20.

6. Conclusions

We have exhaustively studied how the hydrogen electron capture layer expected in the rapidly accreting ($\dot{M} > 10^{-10}M_\odot \text{ yr}^{-1}$) neutron stars affects the internal g-mode spectrum of these objects. The abrupt rise in density across the layer supports a density discontinuity mode (see §4.1) of frequency

$$f_d \approx 35 \text{ Hz} \left(\frac{X_r}{0.1}\right)^{1/2} \left(1 - \frac{\Delta Z}{\Delta A}\right)^{1/2} \left(\frac{10 \text{ km}}{R}\right) \left(\frac{l(l+1)}{2}\right)^{1/2}, \quad (48)$$

where ΔZ and ΔA are the average change in the nuclei's charge and mass through the layer due to neutron captures and subsequent β -decays. The internal buoyancy due to the composition gradient within the electron capture boundary layer creates a new spectrum of “trapped” modes (see §4.2) of frequency

$$f_{tr} \approx \frac{8.5 \text{ Hz}}{n_{tr}} \left(\frac{X_r}{0.1}\right)^{1/2} \left(\frac{10 \text{ km}}{R}\right) \left(\frac{l(l+1)}{2}\right)^{1/2}, \quad (49)$$

where n_{tr} is the number of nodes in the boundary layer and we have omitted the weak dependence on the accretion rate. There is also a set of thermal g-modes in the same frequency range as the trapped modes, which are separated by the density discontinuity into two distinct sets (see §4.3).

This work might eventually provide a natural explanation for some of the observed QPO's in accreting NS. Indeed, if the neutron stars in the “Z” sources were slowly rotating, the discontinuity (trapped) modes from the hydrogen electron capture layer would nicely overlap the frequencies of the QPOs seen in the horizontal (normal) branch. The stable 40 Hz QPO in the $f_s \approx 2$ Hz X-ray pulsar GRO J1744-28 (Zhang et al. 1996) is an intriguing one to consider, as the discontinuity mode is in the right frequency range and might have a small enough shear so that the $\lesssim 10^{11}$ G field of this pulsar (Bildsten & Brown 1997) will not affect the mode frequency. However, there is still much theoretical work to be done, from understanding how the modes are excited to how they modulate the X-ray flux.

6.1. Observational Tests

Observational progress will come by identifying QPOs with modes of different l 's, where the ratio of the mode frequencies are known. This is easiest when the neutron star is rotating slowly (spin frequency $f_s < 10$ Hz), as one then merely looks for the $\omega^2 \propto l(l+1)$ scaling between QPO's that are (ideally) simultaneously present. The rapidly rotating case is more complicated as the angular eigenfunctions and dispersion relations are very different. As we discuss below, seismological progress can most likely be made only for those NS where the spin frequency has been measured during a Type I burst (see Bildsten 1998b for a summary of those objects).

An important question is how fast can the mode frequencies change? The mode frequencies depend on internal conditions in the ocean, in particular on the temperature and X_r . If a QPO was observed to change its frequency faster than the internal conditions in the ocean can change or if the dynamic range of the frequency was too great, this could rule out non-radial oscillations as a source of the periodicity. The discontinuity mode frequency and the trapped mode frequencies are sensitive to the residual hydrogen mass fraction, X_r . This changes from one X-ray burst to another, which will result in layers of different X_r being compressed towards the electron capture boundary layer. These layers are most likely Rayleigh-Taylor unstable and will mix, making the timescale for a large frequency change roughly the accretion time at the transition layer, days to weeks. The thermal modes and trapped modes are sensitive to the temperature in the ocean. The important timescale is the thermal time at the place where most of the mode energy resides, hours to days at the electron capture depth. Thus the upper thermal mode frequencies will change faster than the lower thermal mode frequencies. As we noted in §4, since the thermal time is shorter than the accretion time, the change in the mode frequencies on a short timescale will be determined by the change in the thermal buoyancy and not the structure of the transition layer.

6.2. The Rapidly Rotating Case

There is good reason to suspect that these neutron stars are rapidly rotating, as the prolonged accumulation of material at this rate will most likely spin up the star. The coherent periodicities during Type I X-ray bursts seem to indicate 250–500 Hz spin frequencies, which are much greater than the g-mode frequencies, but still small compared to the breakup frequency $\Omega_b \approx (GM/R^3)^{1/2}$ (≈ 2 kHz for a $1.4M_\odot$, $R = 10$ km star). When $\Omega \ll \Omega_b$, the unperturbed star is spherical and the centrifugal force can be neglected, in which case the primary difference in the momentum equations is the Coriolis force. As a result, the g-mode frequencies depart significantly from the $\omega^2 \propto l(l+1)$ scaling (Papaloizou & Pringle 1978).

BUC96 made progress on this problem within what is called the “traditional approximation”, where the radial and transverse momentum equations separate and the resulting angular equation must be solved to find the angular eigenfunctions (no longer Y_{lm} 's) and transverse eigenvalues $\lambda \equiv kR^2$ (no longer $l(l+1)$). The radial equations are identical to the non-rotating case, so that if ω_0 is the eigenfrequency for the $l = 1$ mode of a *non-rotating* star, then the oscillation frequency (in the rotating frame) at arbitrary spin is $\omega = \omega_0(\lambda/2)^{1/2}$. These are then transferred into the observer's inertial frame via $\omega_I = \omega - m\Omega$, so that going from our non-rotating results to the rotating star is straightforward. However, nearly any frequency can be predicted in the absence of prior knowledge of the spin frequency, as the retrograde modes cover a large frequency range as the NS spin is varied.

Robust predictions are, however, possible for those NSs where the spin frequency is known from a Type I burst. By far the best case to date is 4U 1728-34 (Strohmayer et al. 1996; Strohmayer, Zhang & Swank

1997) which has $f_s = 363$ Hz. For a known spin frequency, BUC96 and Bildsten et al. (1998) have shown that one can predict the observed frequencies as a function of the internal conditions (e.g. T or X_r). Bildsten et al. (1998) asked how the observed frequencies for different angular eigenmodes would change as the internal conditions change. They found that the prograde modes are all at relatively high frequencies, near a kHz. However, these mode frequencies did not exhibit the large dynamic range of the observed kHz QPOs. The splitting for some of the prograde modes was found to be nearly constant, but *not* equal to the spin frequency. Other prograde modes had varying differences and could potentially be applicable to those kHz QPO's that do not have constant frequency separation (Sco X-1, van der Klis et al. 1997, 4U 1608-52, Mendez et al. 1998). Of particular interest were the retrograde modes that appeared at $f < 100$ Hz. These showed a large dynamic range for only a small change in internal conditions. Bildsten et al. (1998) thus pointed to the possibility of explaining some of the QPOs seen in the < 100 Hz range from 4U 1728-34 and other Atoll sources.

Bildsten et al. (1998) pointed out that confirming non-radial pulsations in a star with a previously measured spin frequency can come by identifying a measured low-frequency QPO with a particular value of the non-rotating frequency and then searching in the data for the higher frequency prograde modes. Such an exercise has yet to be carried out and could potentially bear fruit, as few Fourier bins would need to be searched. The dispersion relations are complicated enough that such exercises can only be done in concert with theory. At present, theoretical predictions can most likely be done at the 10% level. Further theoretical work to include general relativistic effects might be needed for the very rapidly rotating stars ($f_s > 500$ Hz) before such an exercise could be carried out in detail, say at the 1% level.

6.3. Future Work on the Capture Layer, Mode Excitation and Coupling to Accretion

There is still much work needed on the physics of the hydrogen electron capture layer. For example, a more realistic calculation would follow several species of heavy nuclei and incorporate neutron capture cross sections and β decay half-lives for each. It is important to carry out some of these calculations, as there is a possible large-scale instability that might develop underneath the layer. After all the electron captures have occurred, the nuclei will, on average, be neutron rich. These nuclei advect downwards and eventually β -decay (they typically are not Fermi blocked) on timescales much longer than days. This may cause a density inversion as the released electrons will decrease the density, possibly leading to a Rayleigh-Taylor instability underneath the hydrogen electron capture zone.

Which modes does the star like to excite? We are presently working on the internal excitation and damping of the adiabatic modes we have presented here. Following the work of SL96, we are starting by considering the excitation of the upper thermal modes, trapped modes and discontinuity modes by the H/He burning layers. Our new understanding of the mode structure will modify the competition between excitation in the burning layers and damping elsewhere in the star that they found. We hope to show that a sub-set of the infinite spectrum of oscillations we have found here will be excited. Finding the steady-state amplitude of the oscillation is beyond the scope of these calculations since it would require going beyond linear order.

How can a mode modulate the X-ray luminosity? There are a few ways one can imagine. One pointed out by Bildsten et al. (1998) for the rapidly rotating case is from direct interaction with the accretion disk, as the g-modes are confined to a narrow equatorial band that would lie in the same plane as the accretion disk. If the NS does not lie inside the last stable orbit, then the disk should run directly into the surface, allowing for potential periodic modulation of the accretion environment. An alternative is to invoke a weak

magnetic field. The mode frequencies are not modified when $B < 10^9$ G (BC95), but the thermal modes have tremendous shear and will thus, at high altitudes, change their nature (Carroll et al. 1986). Whether the resulting outgoing waves can affect the accretion flow remains an open question.

We thank Hendrik Schatz and Michael Wiescher for conversations regarding the nuclear physics, A. Muslimov for suggesting we check for shear instability, and Greg Ushomirsky and Ed Brown for many insightful conversations and comments on the manuscript. This work was supported by the NASA Astrophysics Theory Program through grant NAG 5-2819. L. B. was also supported by the Alfred P. Sloan Foundation.

REFERENCES

- Aizenman, M. L., Smeyers, P., & Weigert, A. 1977, *Astr. Ap.*, 58, 41
- Ayasli, S., & Joss, P. C. 1982, *ApJ*, 256, 637
- Barnett, R. M., et al. 1996, *Phys. Rev.*, D54, 1
- Bildsten, L. 1998a, in “The Many Faces of Neutron Stars”, ed. A. Alpar, L. Buccheri, and J. van Paradijs (Dordrecht: Kluwer), astro-ph/9709094
- Bildsten, L. 1998b, in “Some Like it Hot: Accretion Processes in Astrophysics”, ed. S. Holt & T. Kallman (New York: AIP)
- Bildsten, L. & Brown, E. F. 1997, *ApJ*, 477, 897
- Bildsten, L., Cumming, A., Ushomirsky, G. & Cutler, C. 1998, in “A Half Century of Stellar Pulsation Interpretations: A Tribute to Arthur N. Cox”, ed. P. A. Bradley & J. A. Guzik (San Francisco: PASP), p. 437 (astro-ph/9712358)
- Bildsten, L. & Cutler, C. 1995, *ApJ*, 449, 800 (BC95)
- Bildsten, L., Salpeter, E. E., & Wasserman, I. 1992, *ApJ*, 384, 143
- Bildsten, L., Salpeter, E. E., & Wasserman, I. 1993, *ApJ*, 408, 615
- Bildsten, L., Ushomirsky, G., & Cutler, C. 1996, *ApJ*, 460, 827 (BUC96)
- Blaes, O., Blandford, R., Madau, P., & Koonin, S. 1990, *ApJ*, 363, 612
- Brassard, P., Fontaine, G., Wesemael, F. & Hansen, C. J. 1992, *ApJS*, 80, 369
- Brown, E. F. & Bildsten, L. 1998, *ApJ*, in press
- Carroll, B. W., Zweibel, E. G., Hansen, C. J., McDermott, P. N., Savedoff, M. P., Thomas, J. H., Van Horn, H. M. 1986, *ApJ*, 305, 767
- Caughlan, G. R. & Fowler, W. A. 1988, *Atomic Data Nucl. Data Tables*, 40, 283
- Christensen-Dalsgaard, J. 1981, *MNRAS*, 194, 229
- Cowan, J. J., Thielemann, F. K., & Truran, J. W. 1991, *Phys Rep*, 208, 267
- Cox, J. P. 1980, *Theory of Stellar Pulsation* (Princeton: Princeton Univ. Press)
- Cox, J. P. & Giuli, R. T. 1968, *Principles of Stellar Structure* (New York: Gordon & Breach)
- Farouki, R. T. & Hamaguchi, S. 1993, *Phys. Rev. E*, 47, 4330
- Finn, L. S. 1987, *MNRAS*, 227, 265
- Fujimoto, M. Y., Hanawa, T., & Miyaji, S. 1981, *ApJ*, 247, 267

- Fushiki, I., Taam, R. E., Woosley, S. E., Lamb, D. Q. 1992, *ApJ*, 390, 634
- Gabriel, M. 1980, in *Proc. Workshop on Nonradial and Nonlinear Stellar Instabilities*, ed. H. Hill & W. Dziembowski (New York : Springer), p. 488
- Gudmundsson, E. H., Pethick, C. J., & Epstein, R. I. 1983, *ApJ*, 272, 286
- Haensel, P. & Zdunik, J. L. 1990a, *A & A*, 227, 431
- Haensel, P. & Zdunik, J. L. 1990b, *A & A*, 229, 117
- Hameury, J. M., Bonazzola, S., Heyvaerts, J. & Ventura, J. 1982, *A & A*, 111, 242
- Hanawa, T., Sugimoto, D. & Hashimoto, M. 1983, *PASJ*, 35, 491
- Hansen, C. J. & Kawaler, S. D. 1994, *Stellar Interiors: Physical Principles, Structure and Evolution* (New York: Springer-Verlag)
- Hasinger, G. & van der Klis, M. 1989, *A&A*, 225, 79
- Joss, P. C. 1978, *ApJ*, 225, L123
- Kaaret, P., Ford, E. C. & Chen, K. 1997, *ApJ*, 480, L27
- Kluźniak, W., Michelson, P., & Wagoner, R. V. 1990, *ApJ*, 358, 538
- Kluźniak, W., & Wagoner, R. V. 1985, *ApJ*, 297, 548
- Lamb, D. Q., & Lamb, F. K. 1978, *ApJ*, 220, 291
- Lang, K. R. 1980, *Astrophysical Formulae* (New York: Springer-Verlag), p. 398
- Lewin, W. H. G., van Paradijs, J., & van den Heuvel 1995, *X-Ray Binaries* (London: Cambridge)
- McDermott, P. N. 1990, *MNRAS*, 245, 508
- McDermott, P. N. & Taam, R. E. 1987, *ApJ*, 318, 278
- McDermott, P. N., Van Horn, H. M., & Hansen, C.J. 1988, *ApJ*, 325, 725
- McDermott, P. N., Van Horn, H. M., & Scholl, J. F. 1983, *ApJ*, 268, 837
- Mendez, M. et al. 1998, *ApJ*, in press
- Miller, M. C., Lamb, F. K., & Psaltis, D. 1998, *ApJ*, to appear
- Oda, T., Hino, M., Muto, K., Takahara, M., & Sato, K. 1994, *At. Nuc. Data Tables*, 56, 231
- Osaki, Y. 1975, *Pub. Astr. Soc. Japan*, 27, 237
- Papaloizou, J. & Pringle, J. E. 1978, *MNRAS*, 182, 423
- Reisenegger, A. & Goldreich, P. 1992, *ApJ*, 395, 240
- Rosenbluth, M. N., Ruderman, M., Dyson, F., Bahcall, J. N, Shaham, J. & Ostriker, J. 1973, *Ap J*, 184, 907
- Sato, K. 1979, *Prog. of Theor. Physics*, 62, 957
- Schatz, H. et al. 1997a, to appear in *Physics Reports*
- Schatz, H., Bildsten, L., Gorres, J., Wiescher, M., Thielemann, F.-K. 1997b, in “Intersections Between Particle and Nuclear Physics”, ed. T. W. Donnelly (New York: AIP), p. 987
- Schinder, P. J., Schramm, D. N., Wiita, P. J., Margolis, S. H. & Tubbs, D. L. 1987, *ApJ*, 313, 531
- Stella, L. & Vietri, M. 1998, *ApJ*, 492, L59
- Strohmayer, T. E. 1993, *ApJ*, 417, 273

- Strohmayer, T. E. & Lee, U. 1996, *ApJ*, 467, 773 (SL96)
- Strohmayer, T. E., Zhang, W., Swank, J. H., Smale, A., Titarchuk, L., Day, C., & Lee, U. 1996, *ApJ*, 469, L9
- Strohmayer, T. E., Zhang, W. & Swank, J. H. 1997, *ApJ*, 487, L77
- Taam, R. E., & Picklum, R. E. 1979, *ApJ*, 233, 327
- Taam, R. E., Woosley, S. E., Weaver, T. A., & Lamb, D. Q. 1993, *ApJ*, 413, 324
- Taam, R. E., Woosley, S. E., & Lamb, D. Q. 1996, *ApJ*, 459, 271
- van der Klis, M. 1995, in “X-Ray Binaries”, ed. W. H. G. Lewin, J. van Paradijs & E. P. J. van den Heuvel (London: Cambridge), p. 252
- van der Klis, M. et al. 1997, *ApJ*, 481, L97
- van der Klis, M. 1998, in “The Many Faces of Neutron Stars”, ed. A. Alpar, L. Buccheri, and J. van Paradijs (Dordrecht: Kluwer), astro-ph/9704272
- Van Horn, H. M. & Hansen, C. J. 1974, *ApJ*, 191, 479
- Wallace, R. K., & Woosley, S. E. 1984, in “High Energy Transients in Astrophysics”, ed. S. E. Woosley (New York: AIP), p. 319
- White, N. & Zhang, W. 1997, *ApJ*, 490, L87
- Winget, D. E., Van Horn, H. M., & Hansen, C. J. 1981, *ApJ*, 245, L33
- Woosley, S. E. & Weaver, T. A. 1984, in “High Energy Transients in Astrophysics”, ed. S. E. Woosley (New York: AIP), p. 273
- Yakovlev, D. G. & Urpin, V. A. 1980, *Soviet Astron.*, 24, 303
- Zhang, W., et al. 1996, *ApJ*, 469, L29
- Zhang, W., Strohmayer, T. E., & Swank, J. H., 1997, *ApJ*, 482, L167

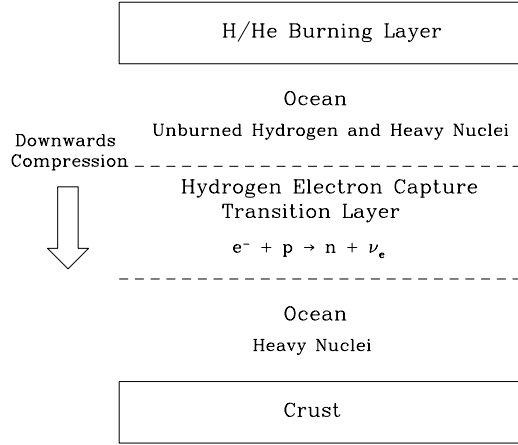


Fig. 1.— A schematic of the atmosphere, ocean and crust of a neutron star accreting at a rapid rate. The accreted H/He burns at a column depth $y \approx 10^8 \text{ g cm}^{-2}$ or a density $\rho \approx 10^{5-6} \text{ g cm}^{-3}$. The ashes from the burning form a degenerate liquid ocean of unburned hydrogen and heavy nuclei. Hydrogen electron captures occur once $E_F = 1293 \text{ keV}$, or $y \approx 10^{10} \text{ g cm}^{-2}$, $\rho \approx 10^7 \text{ g cm}^{-3}$. The thickness of the electron capture transition layer is roughly a scale height. The ocean crystallizes and forms the crust at $y \approx 10^{13} \text{ g cm}^{-2}$, $\rho \approx 10^{9-10} \text{ g cm}^{-3}$. The ocean is nearly isothermal beneath the electron capture transition layer with a temperature of $5-7 \times 10^8 \text{ K}$. For purposes of comparison, the ocean thickness in relation to the radius is about the same as that on the Earth.

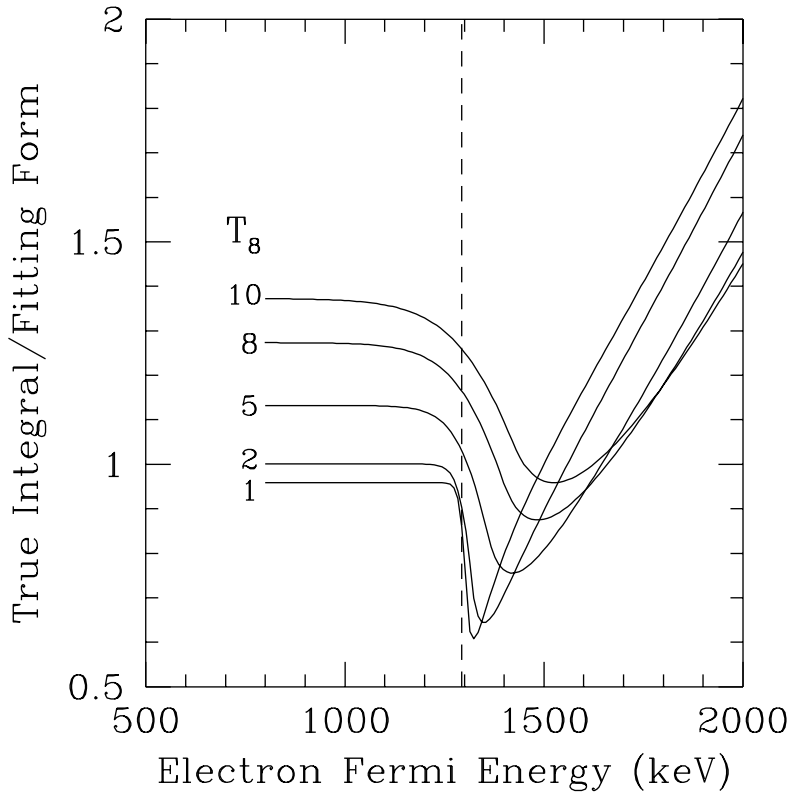


Fig. 2.— The comparison of the exact integral to the analytic fit for the hydrogen electron capture rates. The solid lines show the ratio of the exact integral over the electron energy (eq. [3]) to that determined by our simple analytic fit (eq. [6]) for temperatures of $T_8 = 1, 2, 5, 8$ and 10 . These curves are tabulated and later used to correct the simple formula. The vertical dashed line denotes where $E_F = Q$.

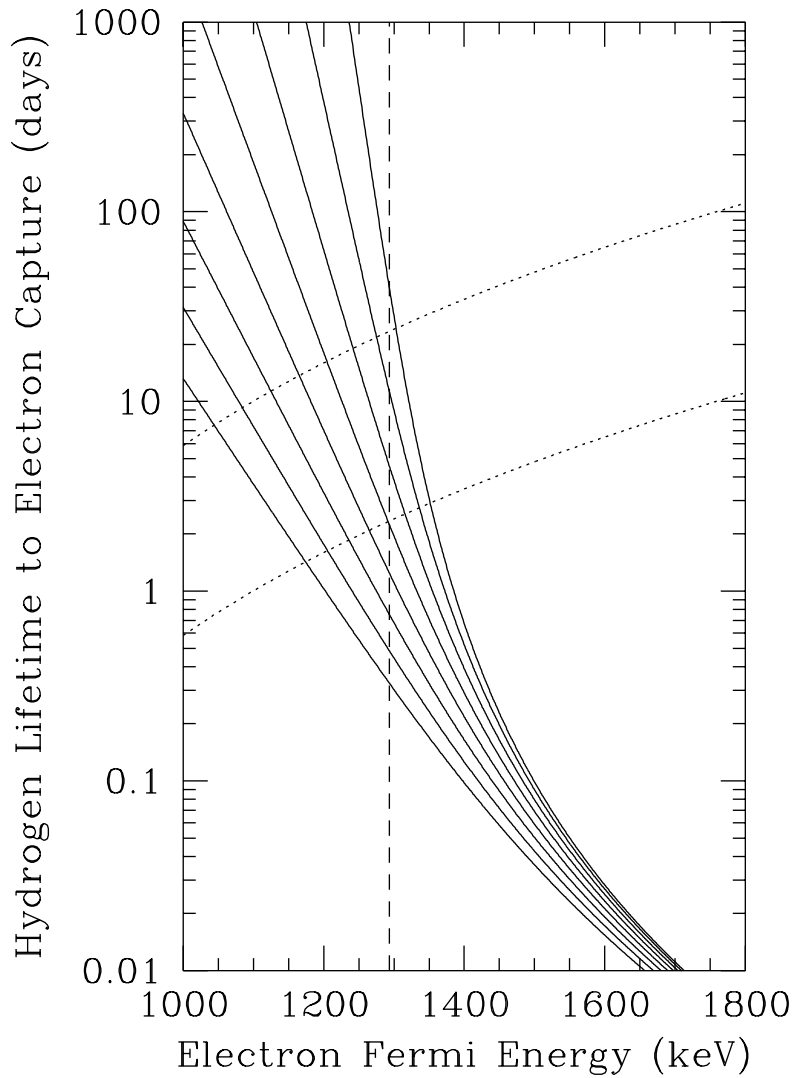


Fig. 3.— The proton lifetime to electron capture as a function of the electron Fermi energy. The solid lines show the lifetime of a proton ($1/R_{ec}$) as a function of the electron Fermi energy for a range of temperatures. Starting from the uppermost solid curve, we display the lifetime for $T_8 = 2, 3, 4, 5, 6, 7, 8$ and 9 . The vertical dashed line denotes where $E_F = Q$. The dotted curves are the rough measure of the time it takes matter to reach that depth for $\dot{m} = \dot{m}_{\text{Edd}}$ (lower dotted) and $\dot{m} = 0.1\dot{m}_{\text{Edd}}$ (upper dotted).

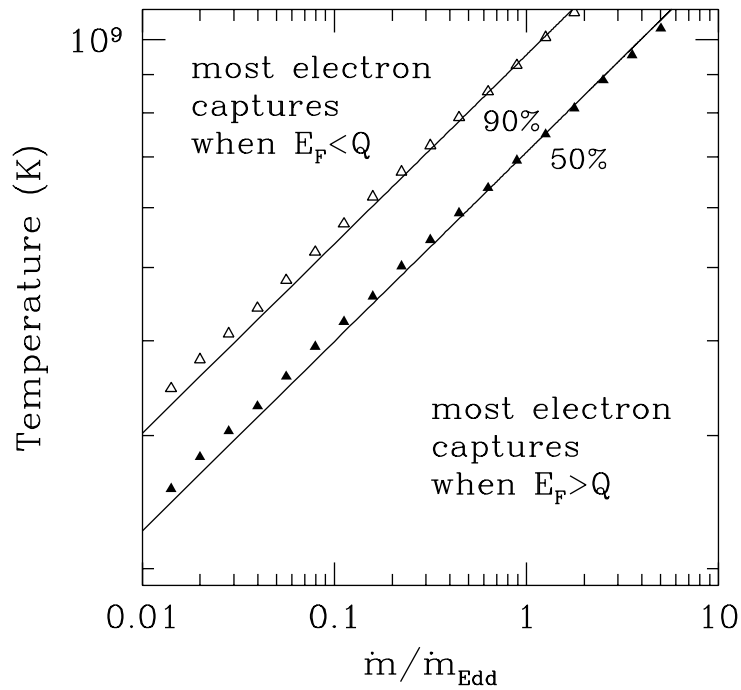


Fig. 4.— Pre-threshold vs. post-threshold electron capture on hydrogen. The \dot{m} - T plane is divided into two regions: at high T or low \dot{m} , most captures happen pre-threshold ($E_F < Q$); at low T or high \dot{m} , most captures happen post-threshold ($E_F > Q$). The filled (open) triangles show points at which 50% (90%) of protons have captured pre-threshold. The solid lines show the $T \propto \dot{m}^{1/4}$ scaling (equation [16]).

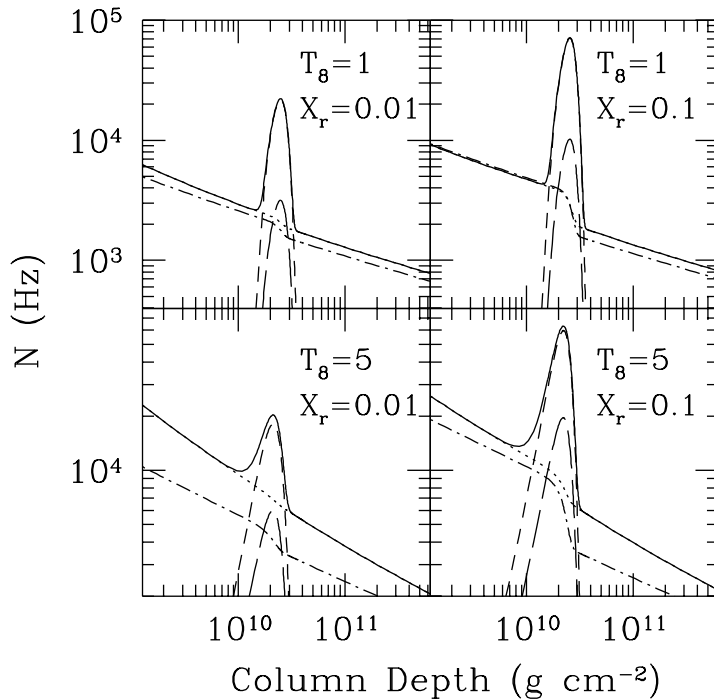


Fig. 5.— The Brunt-Väisälä frequency for isothermal models accreting at $\dot{m} = \dot{m}_{\text{Edd}}$. The solid line shows N , and the different lines show individual contributions. The thermal buoyancy (*dotted line*) dominates above and below the electron capture boundary, while the buoyancy due to the μ_e gradient (*short dashed line*) dominates in the boundary layer. The μ_i buoyancy (*long dashed line*) is about the same as the thermal buoyancy in the layer. The dot-dashed line shows the analytic estimate of the thermal buoyancy (equation (22)), which performs best at low temperatures.

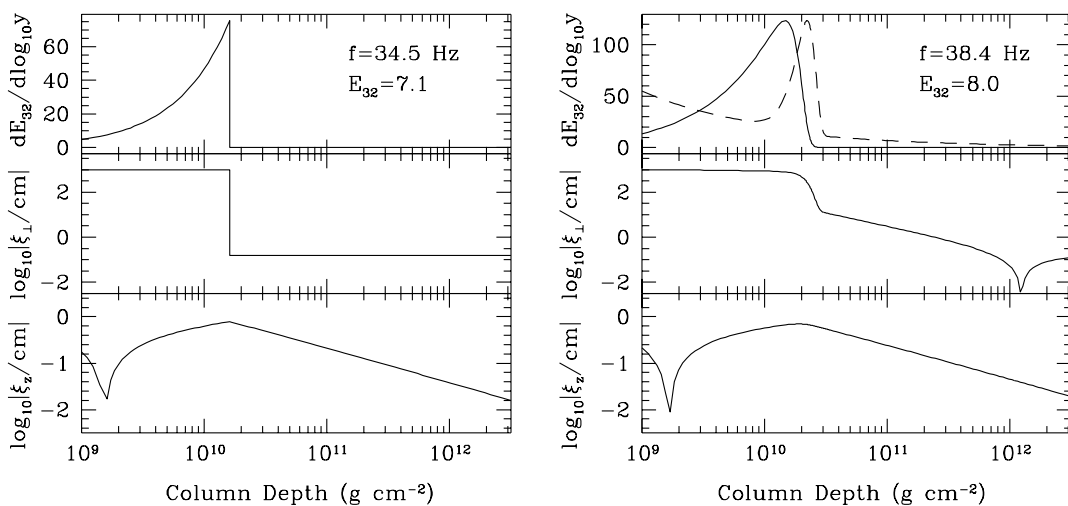


Fig. 6.— Eigenfunctions of the $l = 1$ density discontinuity modes. The left panel shows the density discontinuity mode for a $T = 0$ ocean with $X_r = 0.1$. The right panel is for an isothermal ocean with $\dot{m} = \dot{m}_{Edd}$, $T_8 = 5$ and $X_r = 0.1$. The middle (bottom) panels show the transverse (radial) displacement as a function of column depth. The top panels show the mode energy density $dE_{32}/d\log_{10} y$ (*solid line*) and Brunt Väisälä frequency N on a linear scale (*dashed line*). The displacements shown are absolute values, so zero-crossings appear as cusps. We begin our integrations at a column depth $y = 10^9 \text{ g cm}^{-2}$ and integrate to the floor of the ocean. In all our plots, we arbitrarily normalize the transverse displacement to $\xi_{\perp} = 10^3 \text{ cm}$ at the top of the ocean. The mode energy, E_{mode} , is measured in units of $E_{32} \equiv E_{mode}/10^{32} \text{ erg}$.

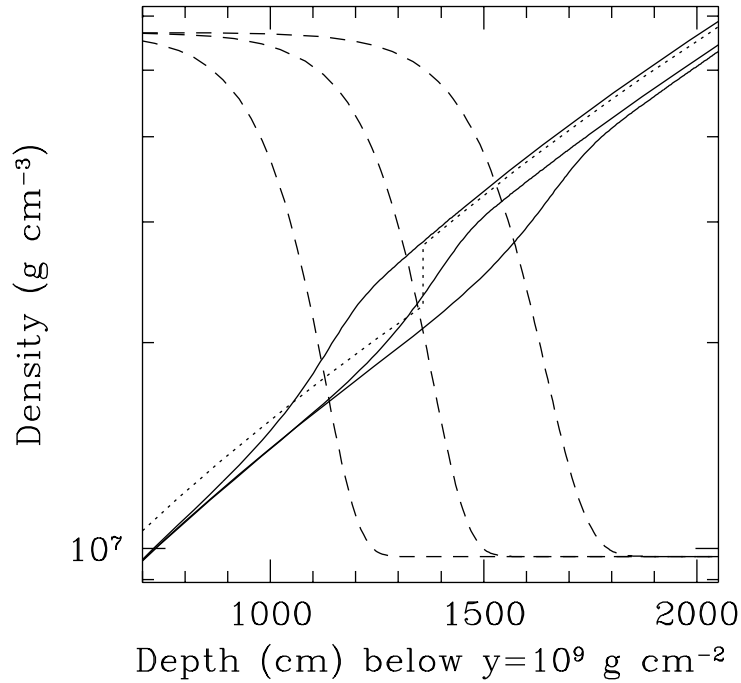


Fig. 7.— Density as a function of depth in an isothermal ocean ($T_8 = 5$) with an initial hydrogen mass fraction $X_r = 0.1$. The solid lines show (left to right) $\dot{m}/\dot{m}_{Edd} = 0.01, 0.1$ and 1 . The dashed lines (left to right) show the hydrogen mass fraction X as a function of depth on a linear scale, with the value at the left being $X_r = 0.1$. The dotted line is for a $T = 0$ completely discontinuous model where all captures occur at $E_F = Q$. The density discontinuity mode for this density profile is shown in the left panel of Figure 6.

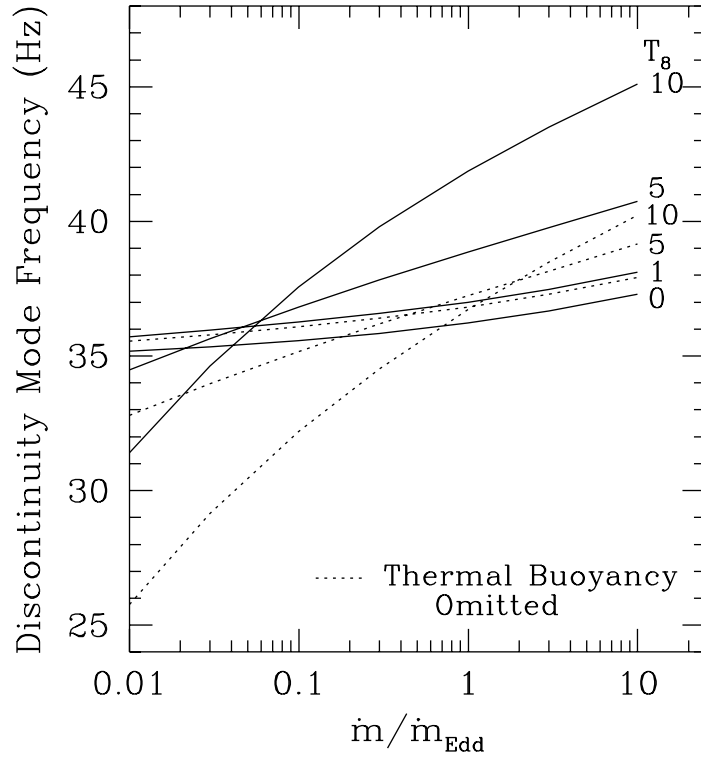


Fig. 8.— The effect of accretion rate and temperature on the $l = 1$ discontinuity mode frequency when $X_r = 0.1$. The solid lines show f_d as a function of \dot{m} for isothermal oceans with $T_8 = 0, 1, 5$ and 10 . The dotted lines show f_d for models where the thermal buoyancy is omitted. At low \dot{m} , f_d decreases with increasing T_8 . This is because pre-threshold captures move the electron capture layer upwards in the ocean, decreasing the scale height at the discontinuity. At high \dot{m} , f_d increases with T_8 because of increasing thermal buoyancy and layer thickness.

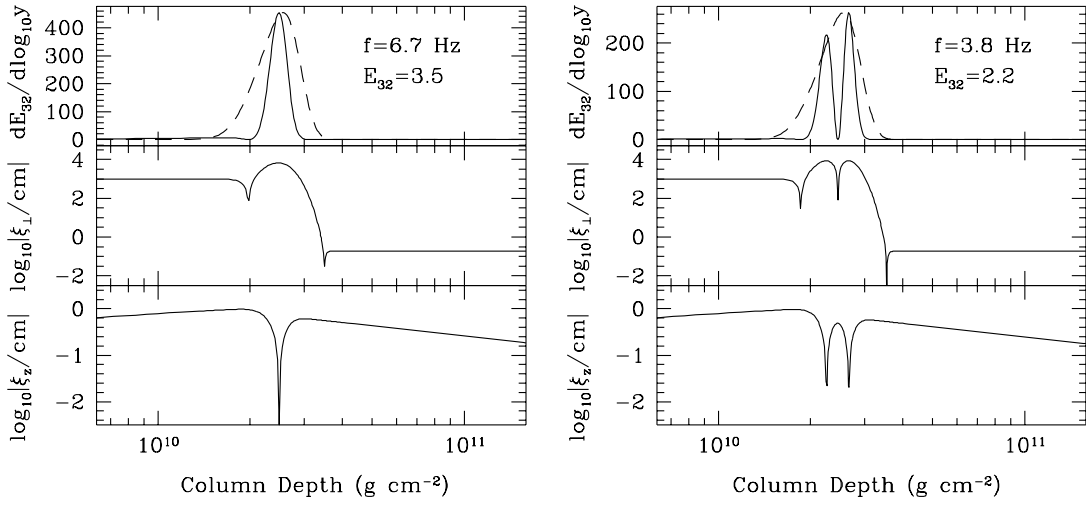


Fig. 9.— The $n_{tr} = 1$ and $n_{tr} = 2$, $l = 1$, trapped modes in a $T = 0$ ocean with $\dot{m} = \dot{m}_{Edd}$ and $X_r = 0.1$. The restoring force for this mode is provided by the μ_e gradient in the electron capture boundary layer. Almost all of the mode energy lies in the boundary layer. Labels and axes are the same as described in Figure 6.

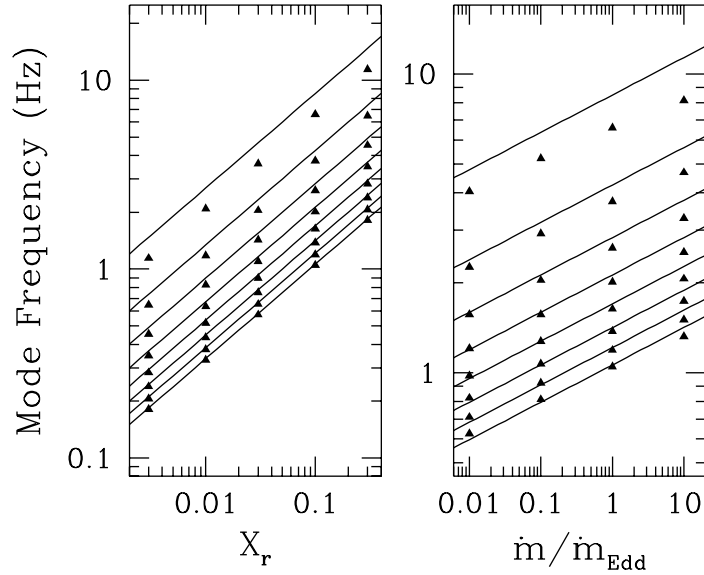


Fig. 10.— The scalings of the $l = 1$ trapped modes with X_r and \dot{m} . The left panel shows the frequencies of the first eight trapped modes ($n_{tr} = 1$ has the highest frequency) in an ocean with $T = 0$ and $\dot{m} = \dot{m}_{\text{Edd}}$ (triangles) compared with the predicted scaling $f_{tr} = 8.5 \text{ Hz } (X_r/0.1)^{1/2}/n_{tr}$ (solid lines). The right panel compares the observed and predicted scaling with \dot{m} , $f_{tr} = 8.5 \text{ Hz } (\dot{m}/\dot{m}_{\text{Edd}})^{1/8}/n_{tr}$, when $X_r = 0.1$ and $T = 0$. There is good agreement, even for small n_{tr} where the WKB approximation doesn't strictly apply. Here n_{tr} is the number of radial nodes within the transition layer.

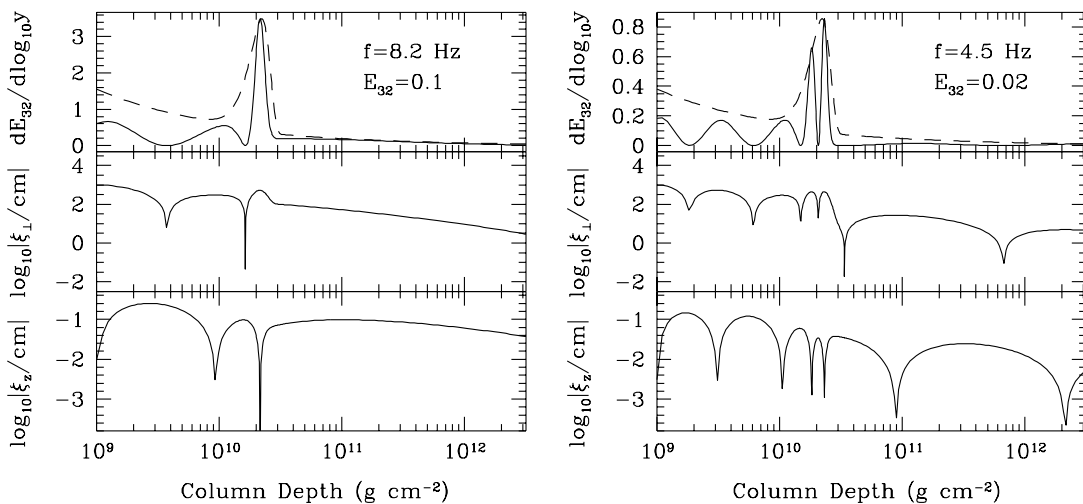


Fig. 11.— The $n_{tr} = 1$ and $n_{tr} = 2$, $l = 1$ trapped modes in an ocean with $T_8 = 5$, $\dot{m} = \dot{m}_{Edd}$ and $X_r = 0.1$. The effect of thermal buoyancy is to allow some of the mode energy to extend into the upper ocean. Labels and axes are the same as described in Figure 6.

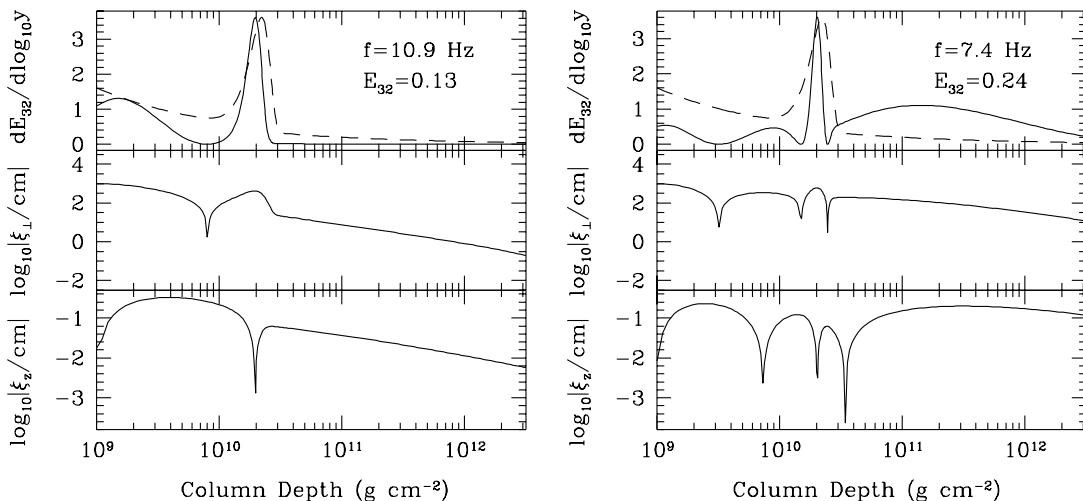


Fig. 12.— Thermal g-mode $l = 1$ eigenfunctions for an isothermal ocean with $T_8 = 5$, $\dot{m} = \dot{m}_{Edd}$ and $X_r = 0.1$. Left (right) panel displays an upper (lower) thermal mode, so called as most of the mode energy resides above (below) the electron capture transition layer. Labels and axes are the same as described in Figure 6.

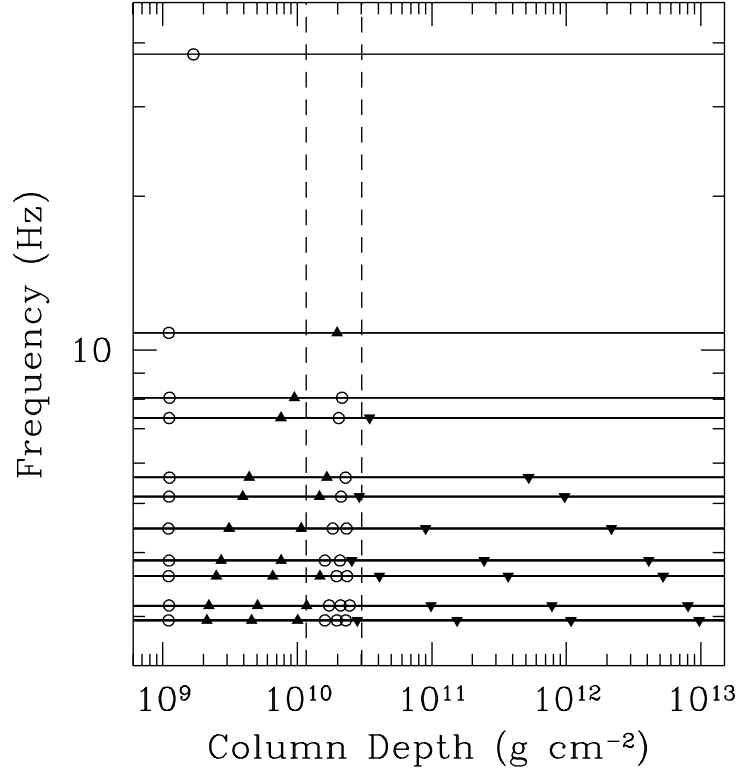


Fig. 13.— The spectrum of $l = 1$ modes in an isothermal ocean with $T_8 = 5$, $\dot{m} = \dot{m}_{Edd}$ and $X_r = 0.1$. Each horizontal line shows a mode frequency. The highest frequency mode is the discontinuity mode, lower frequency modes are trapped and thermal modes. The dashed vertical lines show the places where the thermal and composition gradient contributions to N^2 are equal; these lines show the approximate boundaries of the electron capture layer. Moving down the diagram, each new radial node is marked according to the type of mode, circles for trapped modes and upward-pointing (downward-pointing) triangles for upper (lower) thermal modes. The trapped nodes remain within the boundary layer, whereas the nodes for the upper (lower) thermal modes move upwards (downwards) in the ocean as the frequency decreases. From the top down, the type of modes are d,u,t,l,u,l,t,l,u,t,l, where d is for discontinuity, t is for trapped and u(l) is for an upper (lower) thermal mode. See text for further discussion.

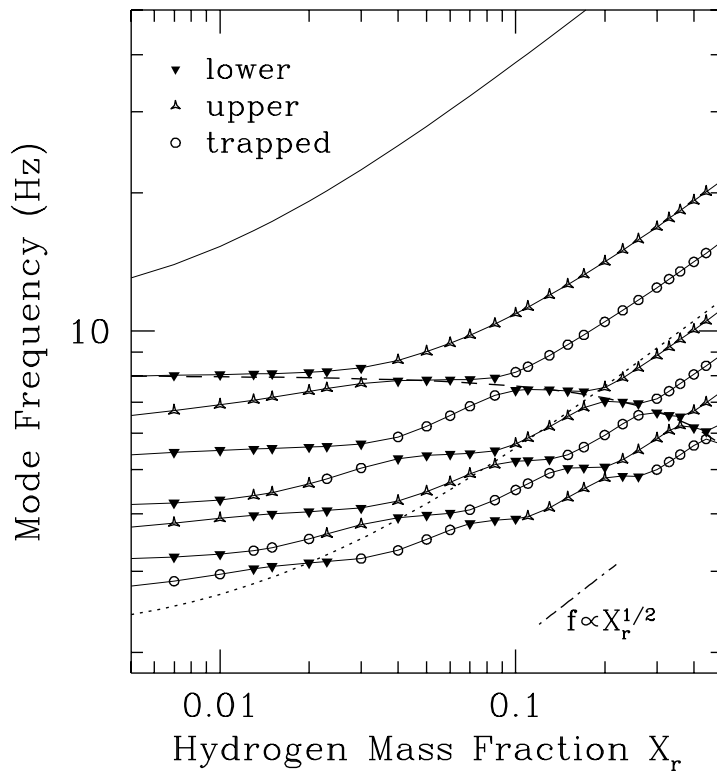


Fig. 14.— The $l = 1$ frequencies of the discontinuity mode and the first few thermal/trapped modes as a function of hydrogen mass fraction X_r in an isothermal ocean with $T_8 = 5$ and $\dot{m} = \dot{m}_{Edd}$. Each solid line is for a mode with a fixed number of radial nodes. The type of mode is shown as a circle (trapped modes) or triangle (thermal modes). The dot-dashed line is the $X_r^{1/2}$ scaling expected for the trapped and discontinuity mode frequencies. The thermal mode frequencies scale as $\mu_i^{-1/2}$. For the lower thermal modes (dashed line) this gives a decreasing frequency with X_r , while for the upper thermal modes (dotted line) the scaling is $\propto X_r^{1/2}$ at high X_r but levels out at low X_r .

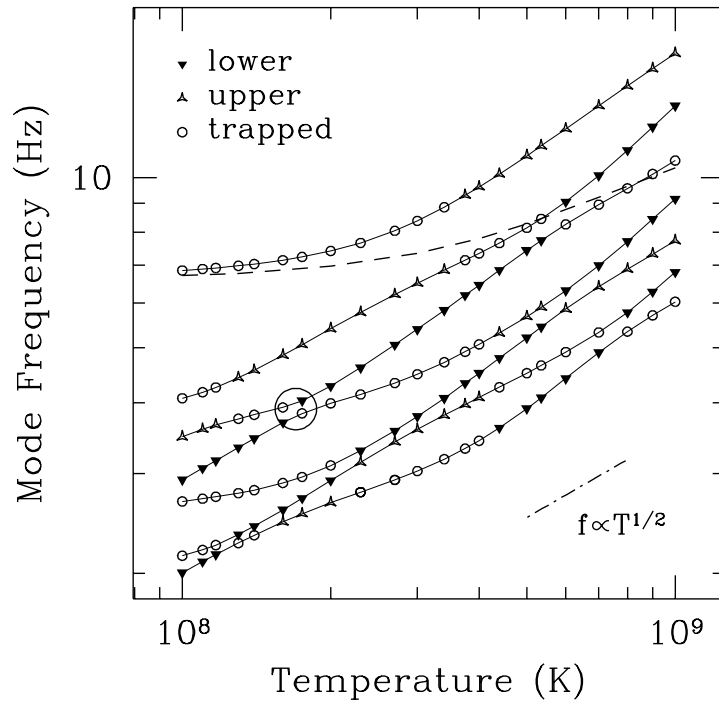


Fig. 15.— The $l = 1$ frequencies of the first few thermal/trapped modes as a function of temperature in an isothermal ocean with $\dot{m} = \dot{m}_{Edd}$ and $X_r = 0.1$. As in Figure 14, each solid line is for a mode with a fixed number of radial nodes, and we show the type of mode by a circle or triangle. The dot-dashed line shows the $T^{1/2}$ frequency scaling of the thermal modes. The dashed line shows the frequency of the $n = 1$ trapped mode when thermal buoyancy is not included. The circled avoided crossing is displayed in detail in Figure 16.

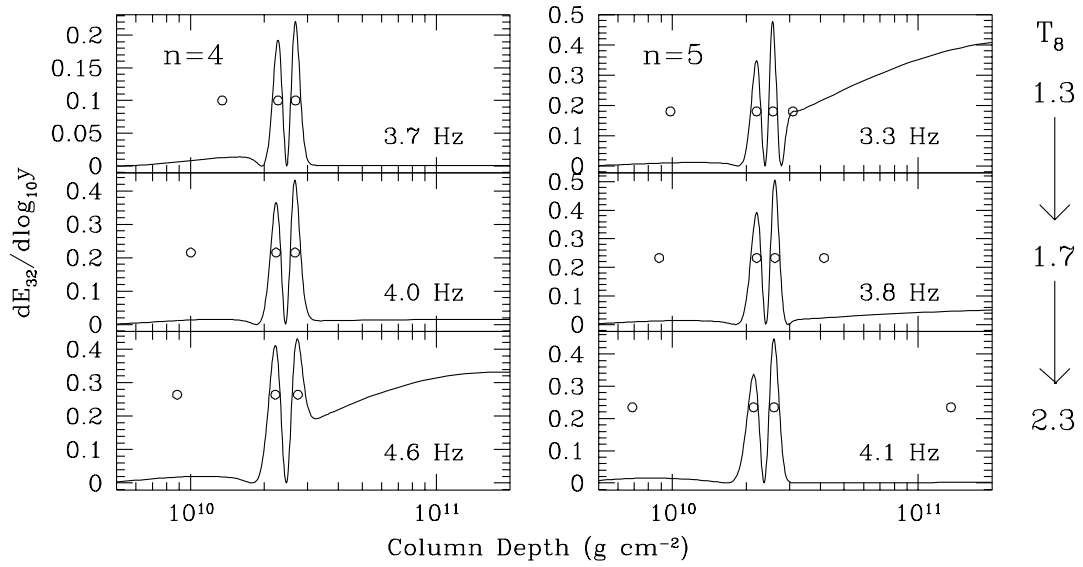


Fig. 16.— The avoided crossing (for $l = 1$) between a trapped and lower thermal mode. The $n = 4$ and $n = 5$ mode energy densities are shown as a function of column depth for a range of temperatures from top to bottom. The circles show the position of the radial nodes. See text for discussion. This avoided crossing is circled in Figure 15.

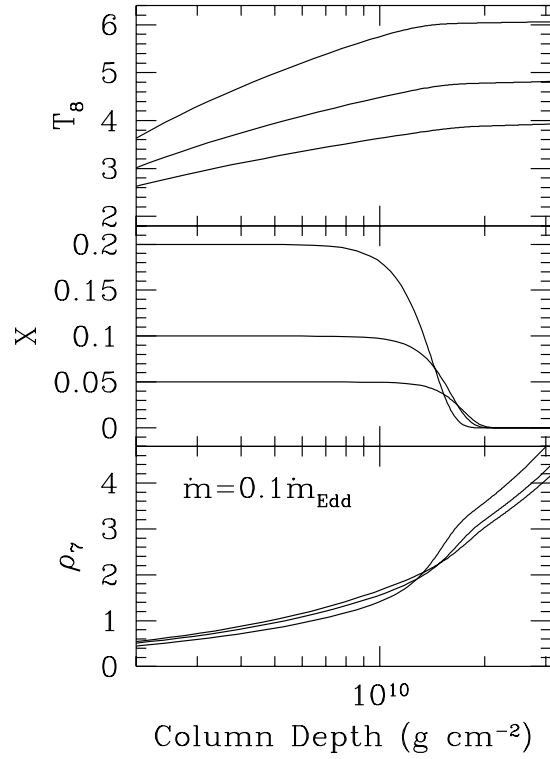


Fig. 17.— The structure of an $R = 10$ km, $M = 1.4M_{\odot}$ NS near the hydrogen electron capture region for an accretion rate of $\dot{m} = 0.1\dot{m}_{\text{Edd}}$ and different values of X_r . The three lines in the top (middle) panel show the temperature in units of 10^8 K (hydrogen mass fraction, X) as a function of the column depth $y = p/g$ for (from top to bottom) $X_r = 0.2, 0.1$ and 0.05 . The bottom panel displays the density (in units of 10^7 g cm $^{-3}$) for the three different values of X_r . The line with the highest density at the highest column is for $X_r = 0.2$.

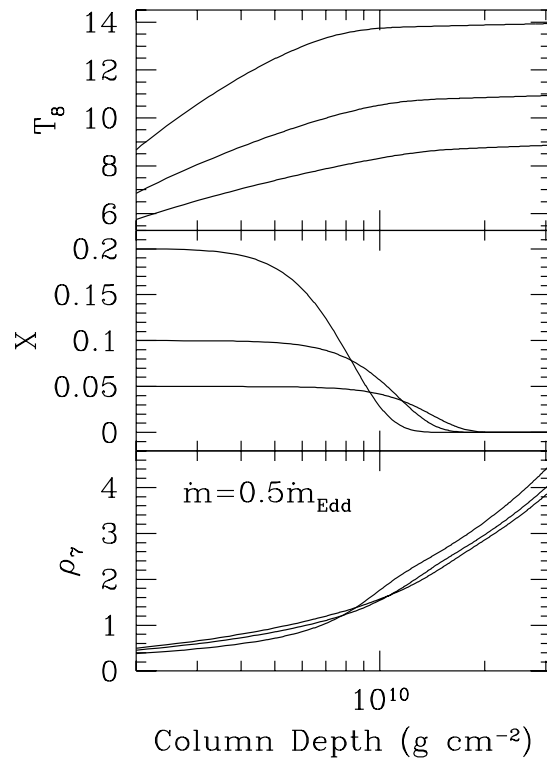


Fig. 18.— The NS structure near the hydrogen electron capture region for $\dot{m} = 0.5\dot{m}_{\text{Edd}}$ and different values of X_r . The labels and arrangement are the same as in Figure 17.

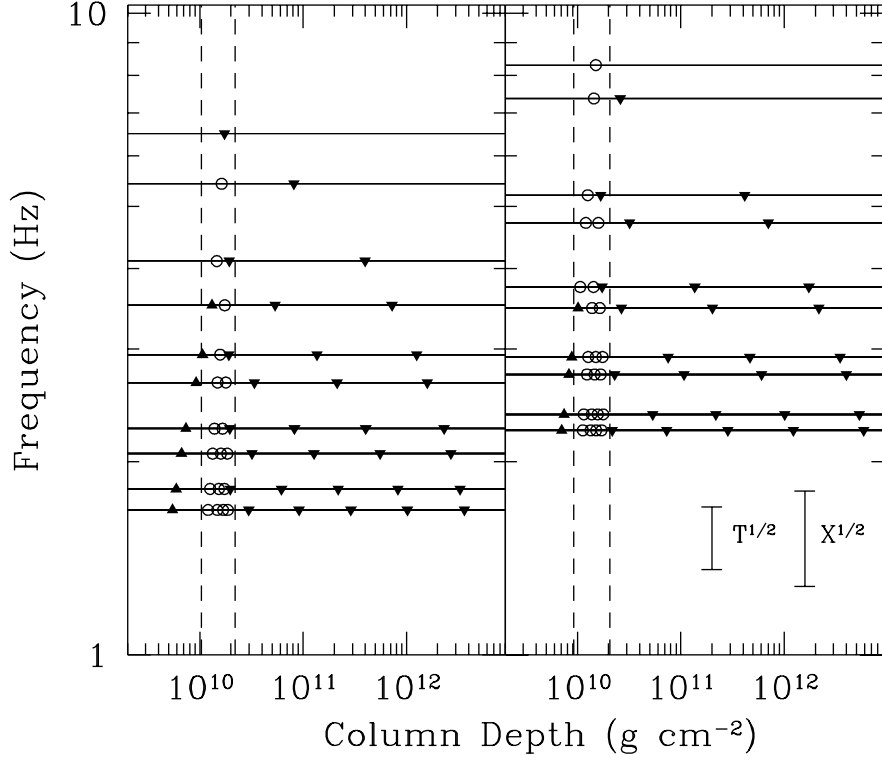


Fig. 19.— The spectrum of $l = 1$ modes in non-isothermal oceans with $\dot{m} = 0.1\dot{m}_{Edd}$ and $X_r = 0.05$ (left panel) and $X_r = 0.1$ (right panel). The temperature at the top ($y = 10^9 \text{ g cm}^{-2}$) is $T_8 = 2$ and rises to $T_8 \approx 4$ ($X_r = 0.05$) and $T_8 \approx 5$ ($X_r = 0.1$) below the electron capture layer (at $y = 3 \times 10^{10} \text{ g cm}^{-2}$). We have included a deep flux of 0.1 MeV per accreted nucleon. The initial nucleus before electron capture has $A_i = 60$, $Z_i = 30$. In each case, we show the discontinuity mode and the first ten trapped and thermal modes. The symbols in this Figure are the same as in Figure 13. For clarity, we have omitted the first radial node which lies near the upper boundary. The vertical bars show the difference in frequency expected between the left and right panels given the simple scalings $X_r^{1/2}$ and $T^{1/2}$.

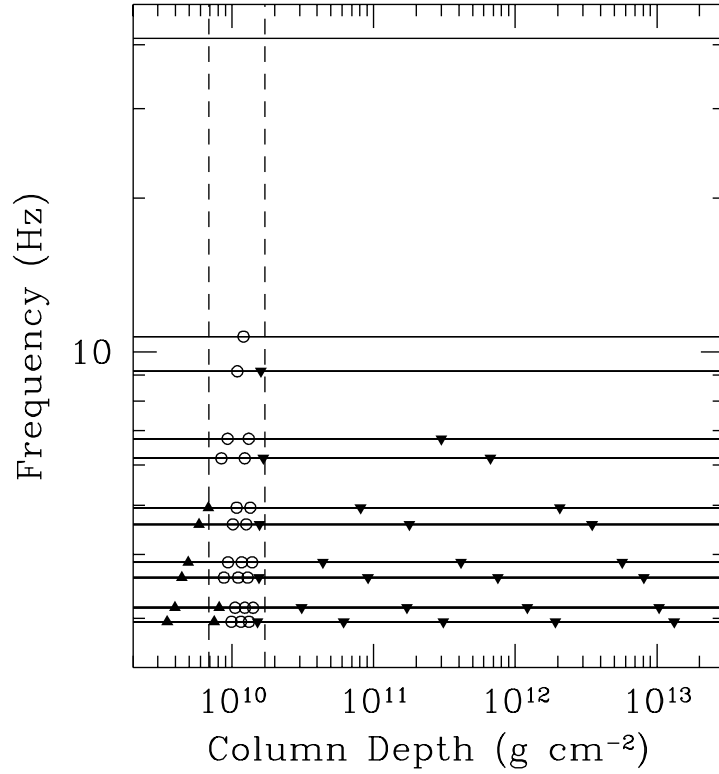


Fig. 20.— The spectrum of $l = 1$ modes in a non-isothermal ocean with $X_r = 0.137$ and $\dot{m} = 0.1\dot{m}_{Edd}$. The temperature at the top ($y = 10^9 \text{ g cm}^{-2}$) is $T_8 = 3.5$ and rises to $T_8 = 5.6$ below the electron capture layer (at $y = 3 \times 10^{10} \text{ g cm}^{-2}$). We have included a deep flux of 0.1 MeV per accreted nucleon. The initial nucleus before electron capture is iron ($A_i = 56$, $Z_i = 26$). This model is based on model 8 of Taam et al. (1996). We show the discontinuity mode and the first ten trapped and thermal modes. The symbols in this Figure are the same as in Figure 13. For clarity, we have omitted the first radial node which lies near the upper boundary. From top to bottom, the modes are d,t,l,t,l,u,l,t,l,u,l, where d is for discontinuity, t is for trapped and u(l) is for an upper (lower) thermal mode.